The Astronomical Journal, 156:295 (24pp), 2018 December https://doi.org/10.3847/1538-3881/aaca35

Warm Molecular Hydrogen in Nearby, Luminous Infrared Galaxies

Andreea O. Petric[1,2], Lee Armus[3], Nicolas Flagey[2], Pierre Guillard[4], Justin Howell[3], Hanae Inami[5], Vassillis Charmandaris[6,7], Aaron Evans[8,9], Sabrina Stierwalt[8,9], Tanio Diaz-Santos[3,10], Nanyao Lu[11,12], Henrik Spoon[13], Joe Mazzarella[3], Phil Appleton[3], Ben Chan[3], Jason Chu[1], Derek Hand[14], George Privon[15], David Sanders[1], Jason Surace[3], Kevin Xu[3], and Yinghe Zhao[3,16,17,18]
[1] Institute for Astronomy, 2680 Woodlawn Drive, Honolulu, HI 96822, USA; apetric@hawaii.edu
[2] Canada–France–Hawaii Telescope, 65-1238 Mamalahoa Highway, Kamuela, HI 96743, USA
[3] Infrared Processing & Analysis Center, MS 100-22, California Institute of Technology, Pasadena, CA 91125, USA
[4] Institut d'Astrophysique de Paris, 96 bis boulevard Arago, F-75014 Paris, France
[5] Universite de Lyon, 92 Rue Pasteur, F-69007, Lyon, France
[6] Department of Physics, University of Crete, GR-71003 Heraklion, Greece
[7] IAASARS, National Observatory of Athens, GR-15236, Penteli, Greece
[8] Department of Astronomy, University of Virginia, Charlottesville, VA 22903, USA
[9] National Radio Astronomy Observatory, 520 Edgemont Road, Charlottesville, VA 22903, USA
[10] Nucleo de Astronomia de la Facultad de Ingenieria, Universitad Diego Portales, Av. Ejercito Libertador 441, Santiago, Chile
[11] National Astronomical Observatories, Chinese Academy of Sciences (CAS), Beijing 100012, People's Republic of China; nanyao.lu@gmail.com
[12] China-Chile Joint Center for Astronomy, Camino El Observatorio 1515, Las Condes, Santiago, Chile
[13] Department of Astronomy, Cornell University, 616A Space Science Building, Ithaca, NY 14853, USA
[14] Department of Physics and Astronomy, University of Hawaii, 200 W. Kawili St., Hilo, HI 96720, USA
[15] Instituto de Astrofisica, Facultad de Fisica, Pontificia Universitad Catolica de Chile, Casilla 306, Santiago 22, Chile
[16] Yunnan Observatories, CAS, Kumming 65011, People's Republic of China
[17] Key laboratory for the Structure and Evolution of Celestial Objects, CAS, Kumming 65011, People's Republic of China
[18] Purple Mountain Observatory, CAS, Nanjing, 210008, People's Republic of China
Received 2017 April 6; revised 2018 April 18; accepted 2018 April 26; published 2018 December 5

Abstract

Mid-infrared molecular hydrogen (H_2) emission is a powerful cooling agent in galaxy mergers and in radio galaxies; it is a potential key tracer of gas evolution and energy dissipation associated with mergers, star formation, and accretion onto supermassive black holes. We detect mid-IR H_2 line emission in at least one rotational transition in 91% of the 214 Luminous Infrared Galaxies (LIRGs) observed with *Spitzer* as part of the Great Observatories All-sky LIRG Survey. We use H_2 excitation diagrams to estimate the range of masses and temperatures of warm molecular gas in these galaxies. We find that LIRGs in which the IR emission originates mostly from the Active Galactic Nuclei (AGN) have about 100 K higher H_2 mass-averaged excitation temperatures than LIRGs in which the IR emission originates mostly from star formation. Between 10% and 15% of LIRGs have H_2 emission lines that are sufficiently broad to be resolved or partially resolved by the high-resolution modules of *Spitzer*'s Infrared Spectrograph (IRS). Those sources tend to be mergers and contain AGN. This suggests that a significant fraction of the H_2 line emission is powered by AGN activity through X-rays, cosmic rays, and turbulence. We find a statistically significant correlation between the kinetic energy in the H_2 gas and the H_2 to IR luminosity ratio. The sources with the largest warm gas kinetic energies are mergers. We speculate that mergers increase the production of bulk inflows leading to observable broad H_2 profiles and possibly denser gas.

Key words: galaxies: active – galaxies: interactions – galaxies: ISM – galaxies: starburst

Supporting material: machine-readable tables, figure set

1. Introduction

Molecular hydrogen (H_2) is the material from which stars form and black holes grow. In turn, young massive stars and active galactic nuclei (AGN) transfer energy to the molecular hydrogen and change its physical conditions. In this paper, we use several approaches to estimate if and how the molecular gas changes on kiloparsec scales in response to changes in the gravitational potential due to galaxy mergers and in response to AGN emission.

In interacting galaxies, large gas-flows move low-metallicity gas from the outer regions of the galaxy toward the center (e.g., Kewley et al. 2010). The timescales for this process seem to be on the order of 1 Gyr: Rupke et al. (2010) find that in the approximate time between first and second passage in a merger, the central metallicity becomes diluted by low-metallicity gas flowing in from the metal-poor outskirts of the merging galaxies. Kinematic signatures in the warm molecular gas may indicate bulk flows on similar timescales.

The amount of interstellar medium (ISM) available for star formation determines a galaxy's evolution. Because star formation is enhanced in interacting galaxies (e.g., Patton et al. 2013), mergers may consume their gas supply at a higher rate than non-mergers (e.g., Mihos & Hernquist 1996; Springel 2000; Hayward et al. 2011). However, observational studies of gas in post-mergers find them to have more neutral hydrogen than non-mergers (e.g., Ellison et al. 2015; Larson et al. 2016).

While there are large variations of gas properties in interacting galaxies (e.g., Haan et al. 2011a; Fernández et al. 2014), mergers may have more cold gas than non-mergers because of inflows from cooled ionized halo gas (Braine & Combes 1993; Ellison et al. 2015). If such inflows include a warm molecular phase, it could take the form of asymmetric

Table 1
H_2 Rotational Transitions[a]

Notation[b]	Transition[c]	Rest λ μm[d]	E_u/k (K)[e]	A (10^{-7} s^{-1})[f]	g (J)[g]
S(0)	$J = 2$–0	28.219	510	0.00029	5
S(1)	$J = 3$–1	17.035	1015	0.00476	21
S(2)	$J = 4$–2	12.279	1682	0.0276	9
S(3)	$J = 5$–3	9.665	2504	0.0984	33
S(4)	$J = 6$–4	8.025	3474	0.264	13
S(5)	$J = 7$–5	6.910	4586	0.588	45
S(6)	$J = 8$–6	6.109	5829	1.14	17
S(7)	$J = 9$–7	5.511	7197	2.00	57

Notes.
[a] Roussel et al. (2007).
[b] Short notation of H_2 transition.
[c] The quantum numbers associated with the upper and lower energy levels, the transition from the upper to lower level results in the emission of the observed line listed in column 1.
[d] Rest wavelength for transition given in column 1.
[e] The rotational upper energies from (Black & Dalgarno 1976; Huber & Hertzberg 1979; Roussel et al. 2007).
[f] Transition probabilities from (Black & Dalgarno 1976; Roussel et al. 2007).
[g] The statistical weight for the transition given in column 1.

emission profiles or redshifted components. In this work, we aim to complement studies of atomic hydrogen in mergers, and to trace the fate of the warm molecular gas component in the ISM of nearby star-forming galaxies.

Our investigation focuses on warm molecular gas as traced by H_2 rotational emission lines (Table 1) in a sample of nearby, Luminous Infrared Galaxies (LIRGs). LIRGs are galaxies with $L(8\text{–}1000\ \mu\text{m}) = L_{\rm IR} \geqslant 10^{11}\,L_{\odot}$, a subset of which have $L_{\rm IR} \geqslant 10^{12}\,L_{\odot}$ and are called Ultraluminous Infrared Galaxies (ULIRGs) (Sanders & Mirabel 1996). Because LIRGs can have a wide range of optical classifications and because they span the full range of galaxy interactions from non-merging spirals to late-stage mergers, they are well-suited to the study of how AGN and mergers impact the ISM (Armus et al. 2009; Petric et al. 2011; Stierwalt et al. 2013; Privon et al. 2015; Larson et al. 2016; Psychogyios et al. 2016). Furthermore, LIRGs bridge the luminosity gap between nearby star-forming galaxies and quasars, and therefore they may provide the link between the extreme objects we see at high redshift and normal nearby galaxies.

The LIRGs we study here are part of the Great Observatories All-sky LIRG Survey (GOALS), which targets a representative sample of 202 systems in the local universe ($z \leqslant 0.088$) selected from the *IRAS* Revised Bright Galaxy Sample (Sanders et al. 2003). An outline of the GOALS project and a multiwavelength analysis of the LIRG VV 340 are given in Armus et al. (2009). Results from the MIR spectroscopy of the GOALS sample were presented in Evans et al. (2008), Inami et al. (2010), Díaz-Santos et al. (2010, 2011, 2014), Petric et al. (2011), Mazzarella et al. (2012), Modica et al. (2012), Stierwalt et al. (2013), and Stierwalt et al. (2014).

The connections between processes associated with AGN, merger stage, and the state of the gas are complex. In a detailed, high-spectral resolution, *Spitzer* Infrared Spectrograph (IRS), study of the GOALS LIRGS, Inami et al. (2013) found no correlation between fine-structure line ratios and the merger stage, but did find that emission lines from more highly ionized ions have broader line widths, e.g., [Ne V] emission lines are broader than [Ne III] lines, which in turn are broader than [Ne II] lines. They also find five LIRGs whose shifted [Ne III] and [Ne V] lines suggest the presence of fast-moving, highly ionized gas that may be part of galactic bulk-flows. In this paper, we compare the line widths of the warm molecular gas with the contribution of the AGN to the mid-infrared (MIR) luminosity to test whether the thermal energy in the warm gas is contributed by AGN.

In most LIRGs and ULIRGs, star formation dominates the heating of H_2 (Higdon et al. 2006; Hill & Zakamska 2014; Stierwalt et al. 2014). However, a fraction of LIRGs and an even larger fraction of ULIRGs have more MIR H_2 emission than what could be expected if the H_2 emission originates in photodissociation regions. Stierwalt et al. (2014) use low-resolution IRS data to study the H_2 and dust properties of LIRGs and find that most nearby LIRGs have higher ratios of $L(H_2)/L(\text{PAHs})$ than normal star-forming galaxies. Stierwalt et al. (2014) show that this ratio increases with H_2 luminosity and that, in around 10% of LIRGs, the H_2 emission may be excited by shocks either from powerful starbursts or AGN. On average, ULIRGs have three times more emission in the rotational transitions of molecular hydrogen than expected based on their star formation rates (Hill & Zakamska 2014). Hill & Zakamska (2014) found a strong correlation between [H_2] and [Fe II] suggesting that the excess H_2 is produced by shocks but only by a weak positive correlation between [H_2] emission and the length of the tidal tails, which further suggests that the shocks were not solely associated with mergers.

Studies of warm molecular H_2 kinematics may help disentangle the impact that gravitational interactions and AGN have on the ISM. In this paper, we extract kinematic information from resolved H_2 line profiles to test whether mergers lead to bulk gas motions. We also estimate if and how the masses, temperatures, and excitation conditions of H_2 change with merger stage and with the AGN contribution to the LIRG's IR luminosity. The paper is organized as follows. In Section 2, we describe the IRS observations and reduction methods. Section 3 includes a presentation of the H_2 flux measurements, a description of the method used to estimate the total warm H_2 masses and temperatures, and basic statistics of these quantities as a function of merger stage, IR luminosity, and AGN contribution to the IR emission. In Section 4, we discuss our findings, and we summarize our conclusions in Section 5.

2. Sample and Data

The GOALS sample properties and selection are described in detail in Armus et al. (2009). For this investigation, we use the spectra of 248 individual nuclei in 202 LIRG systems, observed in the high-resolution IRS modules (Short-High and Long-High; abbreviated SH and LH) and complementary low-resolution (IRS Short-Low and Long-Low; abbreviated SL and LL) spectra for 234 sources. The widths of the SL, SH, LL, LH slits (3.″6, 4.″7, 10.″7, 11.″1) correspond to 1.5, 2.0, 4.5, and 4.6 kpc, respectively, at a distance of 88 Mpc—the median galaxy distance in our sample. The distances to the GOALS galaxies are between 17.5 and 387 Mpc. We obtained the IRS spectra in our own observing program (PI: Armus, PID 30323) for 158 LIRG systems, with the IRS spectra for the remaining 44 LIRG systems taken from the *Spitzer* archive. In all data from PID 30323, the IRS Staring Mode was employed, using "cluster target" observations for those sources with well-separated ($\geqslant$10 arcsec) companions. Among the 202 LIRGs studied, secondary nuclei were targeted only when the flux

ratio of primary to secondary nucleus (as measured in the *Spitzer* MIPS 24 μm data) is less than or equal to five, in order to capture the spectra of the nuclei actively participating in the far-infrared emission of the system.

A more detailed description of how the spectra used for the analysis presented in this paper were reduced is given in three previous papers: Petric et al. (2011), Inami et al. (2013), Stierwalt et al. (2013). The spectra were extracted with the SPICE[19] software, assuming that the flux in the slit originates from a point source. The profile for the extraction is set automatically to match the PSF at different wavelengths. The PSF was determined by the IRS team from standard calibrators. Twenty-eight systems were observed in spectral mapping mode. These data were assembled and cleaned to remove noisy pixels. Nuclear spectra were then extracted with CUBISM (Smith et al. 2007a), using extraction regions of sizes equal to those of extraction regions for point sources in the spectra taken in staring mode. More detailed descriptions of the spectra, including the positions of the IRS slits, are given in Stierwalt et al. (2013), Inami et al. (2013), and the GOALS delivery documents (https://irsa.ipac.caltech.edu/data/GOALS/overview.html).

The GOALS sources were classified in five merger stages: (0) no obvious sign of a disturbance in the IRAC or *HST* morphologies, or published evidence that the gas is not in dynamical equilibrium (i.e., undisturbed circular orbits); (1) early stage, where the galaxies are within 1 arcmin of each other, but little or no morphological disturbance can be observed; (2) the galaxies exhibit bridges and tidal tails but do not have a common envelope, and each optical disk is relatively intact; (3) the optical disks are completely destroyed, but two nuclei can be distinguished; (4) the two interacting nuclei are merged, but structure in the disk indicates that the source has gone through a merger. The merger classifications for LIRGs are published in Stierwalt et al. (2013); see also Figure 10 in Petric et al. (2011). A subset of 65 LIRGs was re-evaluated by Larson et al. (2016). We acknowledge the pitfalls of morphological classifications and refer the reader to the more precise techniques requiring high sensitivity and high spatial and velocity resolution (Privon et al. 2013).

Here, we seek to be consistent with previous merger-class investigations of the GOALS sample of LIRGs presented in Larson et al. (2016), Stierwalt et al. (2013), and Haan et al. (2011b). We compress the merger stages into three categories: non-mergers (nm), which are targets without obvious signs of morphological disturbances; early mergers (em), which are systems in which the interacting galaxies are within 1 arcmin of each other but show little or no morphological disturbance; and mergers (m), which include all the other stages of gravitational interactions.

3. Results

In this section, we will present our measurements of emission line fluxes and line widths, how we identify resolved emission lines, and how we estimate warm molecular H_2 masses, temperatures, ortho-to-para ratios (OPR), and H_2 excitation conditions.

[19] http://irsa.ipac.caltech.edu/data/SPITZER/docs/dataanalysistools/tools/spice/spiceusersguide/SPICE_Users_Guide.pdf

3.1. Fluxes

To measure line fluxes and line-widths from our SH, LH, and SL spectra, we fit Gaussian functions to the atomic and molecular gas emission line profiles. We inspect all the fits to ensure that spurious hot pixels were excluded. We did not use PAHFIT (Smith et al. 2007b) because it does not account for potential ice absorption. We also refer the reader to Stierwalt et al. (2014), who present H_2 fluxes estimated from simultaneous fits of the dust and gas features and continuum in the low-resolution data after scaling the SL spectra to match the LL data. Here, we chose to measure the H_2 emission line fluxes the same way from the low- and high-resolution spectra because the S0 line is not easily detected in the low-resolution spectra, yet its measurement is important for determining warm molecular gas mass and temperatures.

For each line flux measurement, we average the fluxes estimated from the two IRS nods; to assess the flux errors, we combine the uncertainties from the Gaussian fits in quadrature. We calculate each upper limit from line-free regions near the line of interest as the total emission for a hypothetical line with a width equal to the spectral resolution at that wavelength and a 3σ intensity peak.

Figure 1 shows the H_2 S(0), S(1), S(2), S(3), [Fe II], [Ne II], [O IV], and [Si II] fluxes measured from IRS spectra. These plots show Nod 1 versus Nod 2 fluxes and Nod 1 fluxes versus the final flux for each of the detected lines. For most of the sources, our estimates from each of the IRS node positions match well. For lines where the flux from the two nods differed by more than $3 \times \sqrt{(\sigma F1^2 + \sigma F2^2)}$, where $\sigma F1$ and $\sigma F2$ respectively represent the errors on the flux measured in Nod 1 and Nod 2, we choose results from the fit with the best overall signal-to-noise ratio (S/N). In addition, we visually reinspect the spectra in order to ensure the fit we use is better than the one we discard and to understand the reason for the difference between the two nods.

Table 2 gives the H_2 rotational emission line fluxes and uncertainties, measured from the IRS high-resolution spectra. Figure 2 shows histograms of the line fluxes and luminosities corresponding to the rotational transitions, S(0), S(1), and S(2). Table 3 gives detection statistics for the H_2 emission lines: percentages of detected sources, minimum, mean, median, maximum, and standard deviations of the detected fluxes and luminosities. In particular, we find that the median H_2 S(0), S(1), and S(2) luminosities are $10^{6.7}$, $10^{7.1}$, and $10^{6.8}\,L_{\odot}$, respectively. Appendix A describes how we combined fluxes from different modules.

3.2. Resolved Lines

The IRS high-resolution modules are described in the official instrumental handbook[20] as cross-dispersed echelle spectrographs that provide a resolving power $R = \lambda/\Delta\lambda \sim 600$. The velocity resolution of the high-resolution modules is nominally $c/R = 494\,\mathrm{km\,s^{-1}}$ between 4 and 18 μm and $503\,\mathrm{km\,s^{-1}}$ between 25 and 34.2 μm. Previous investigations of high-resolution line profiles used measurements of the widths of standard IRS calibration targets (P Cygni, HD 190429, HD 174638) to assess that the uncertainty in the instrumental

[20] (Version 5.0, last modified 2012 December 12).

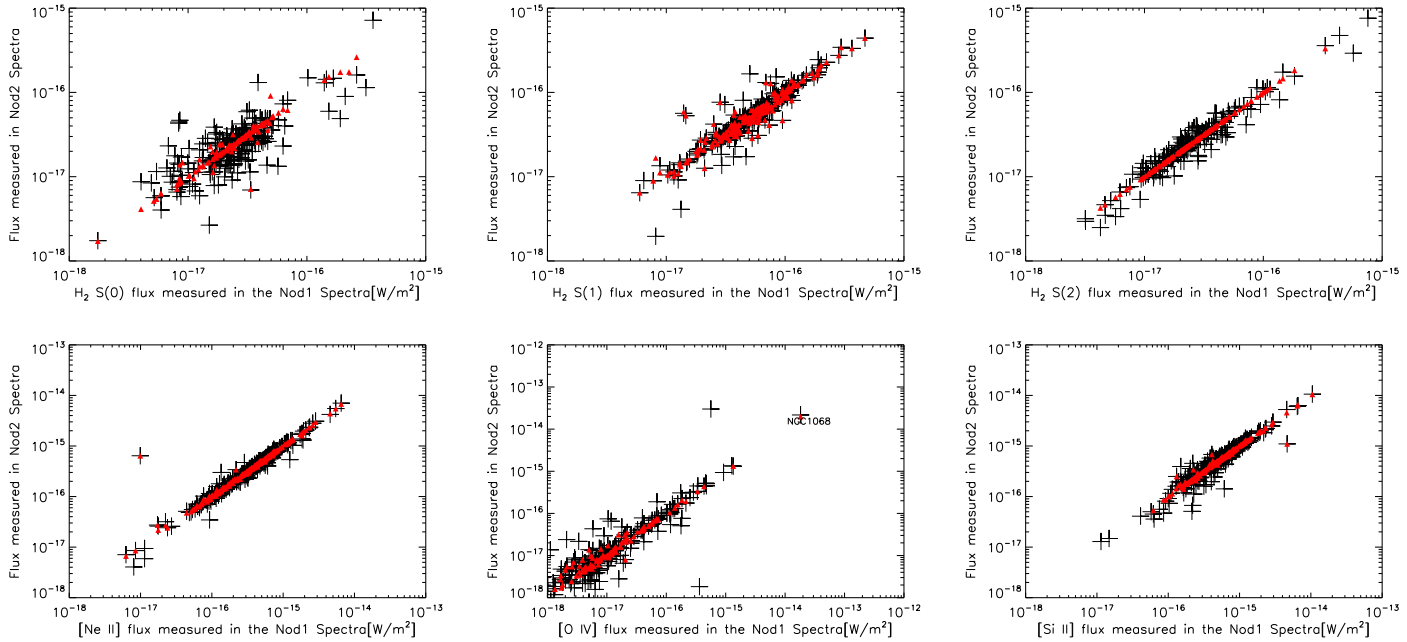

Figure 1. H2 (S0), H2 (S1), H2 (S2), [Ne II], [O IV], and [Si II] fluxes measured from IRS spectra modules SH and LH. As described in the text, each fit was inspected by hand and the continuum adjusted for bad pixels in the two nods associated with each SH or LH observation. These plots show the measured Nod 1 vs. Nod 2 fluxes in black and the Nod 1 fluxes vs. the final flux in red, for each of the detected lines.

resolution is 59 km s^{-1} in SH and 63 km s^{-1} in LH (e.g., Dasyra et al. 2008; Guillard et al. 2012).

To take advantage of the large number of high-resolution, high-S/N spectra of the GOALS targets, here we take a complementary approach and look at the distribution of line widths of the H_2 S(1) and S(0) lines in our sample of LIRGs. To determine the expected distribution of widths for a sample of unresolved sources, we use two independent methods and compare our results. We include several derived line-width estimates that are smaller than the instrumental resolution—those are sources with poor sampling and/or low signal-to-noise ratio. We keep them here because they indicate the error budget in our overall measurements.

Method 1: We assume that, in the absence of resolved sources, the distribution of H_2 line widths should be symmetric. Figure 3 shows the histogram of the H_2 S(1) and S(0) lines with 10 km s^{-1} bins. The distributions of derived line widths show a tail of sources with larger line widths, presumably representing the resolved and marginally resolved objects. We estimate the standard deviation and mode from measurements with an S/N of three or better.

We find that the H_2 S(1) distribution has a mode of 511 km s^{-1} (RES1 hereafter) and a weighted mean of 540 km s^{-1}. Using the mode and the measurements of lines lower than the mode, we obtain a standard deviation of 56 km s^{-1} for the unresolved sources, which we claim is purely of instrumental origin ($\sigma_{\rm inst} = 56$ km s^{-1}). The value for this standard deviation is almost identical to the uncertainty quoted by Dasyra et al. (2008). We look at three classes of sources: clearly resolved, marginally resolved, and unresolved.

By writing FWHM $- \sigma_{\rm FWHM} \geqslant$ RES1$+n$ $*\sigma_{\rm inst}$, where FWHM is the measured full width at half maximum, we find three sources with $n = 3$ and six with $n = 2$. We refer to these sources as being clearly resolved. Eighteen nuclei have marginally resolved H_2 S(1) emission with $n = 1$. Those eighteen marginally resolved sources would have been considered clearly resolved in earlier studies (e.g., Dasyra et al. 2008; Guillard et al. 2012). We present the measured properties of all these 27 sources with FWHM $- \sigma_{\rm FWHM} \geqslant 567$ km s^{-1} in Table 4. Note that these sources are not resolved at a 1σ statistical significance level, but are higher levels, because we look at both the distribution of possible widths and the error associated with each measurement.

Method 2: In the second approach, we derive the distribution of possible measurements for an unresolved source from the measured H_2 line widths (FWHM) and the errors associated with those individual measurements. Figure 4 shows the distribution of derived H_2 S(1) FWHM, each represented as a Gaussian centered on the measured H_2 line width and a width equal to the estimated error on the measurement. Each Gaussian is normalized to an area of 1. Adding up all the individual Gaussian distributions gives the most probable line-width measurement. Adding up all the individual Gaussian distribution of sources with measured H_2 FWHM smaller than this value gives the probability distribution of possible measurements of H_2 line width for an unresolved source. Using this probability distribution and the error on each measurement for the sources we marked as marginally resolved or resolved from the previous technique, we compute the likelihood it is actually unresolved. We find that the sources we marked as marginally resolved and resolved have a probability between 2×10^{-6} (for NGC 6240) and 0.1 (for VV250) to be unresolved with a median value of 0.01.

The S(0) line-width distribution was more difficult to characterize because of larger error bars on the estimated line widths. We found different modes when we binned the line-width distribution using bin sizes of 10, 15, 20, and 25 km s^{-1}. The modes we find range between 421 and 545 km s^{-1}, with an average value of 494 km s^{-1}. The weighted mean of the unbinned distribution of line widths is also 494 km s^{-1}. We thus used the weighted mean of 494 km s^{-1} as the most likely value for a measurement of an unresolved source. The associated dispersion is 62 km s^{-1}. We find eight galaxies that have marginally resolved S(0) lines: NGC 0828, ESO 255-IG007, ESO 507-G070, IRAS 13052-5711, NGC 5257, CGCG

Table 2
H_2 Fluxes

Name	RA deg	Dec deg	S(0) Flux 10^{-18} Wm^{-2}	S(1) Flux 10^{-18} Wm^{-2}	S(2) Flux 10^{-18} Wm^{-2}	S(3) Flux 10^{-18} Wm^{-2}	Merger stage[a]
NGC0023	2.4723	25.924	14 ± 3	96 ± 4	46 ± 8	99 ± 3	*em*
NGC0034	2.7778	−12.107	40 ± 9	139 ± 7	41 ± 5	58 ± 1	*m*
Arp256	4.7121	−10.377	<8	48 ± 6	18 ± 5	25 ± 2	*m*
ESO350-IG038	9.2189	−33.555	<9	8 ± 1	<6	<30	*m*
NGC0232-W	10.6910	−23.561	18 ± 3	108 ± 6	46 ± 11	105 ± 2	*em*
NGC0232-E	10.7201	−23.541	<7	52 ± 6	13 ± 6	61 ± 6	*em*
MCG+12-02-001	13.5162	73.085	70 ± 3	92 ± 5	32 ± 8	83 ± 3	*m*
NGC0317B	14.4184	43.792	53 ± 4	107 ± 5	40 ± 8	57 ± 11	*m*
IC1623B	16.9482	−17.507	101 ± 5	190 ± 2	88 ± 4	50 ± 1	*m*
MCG-03-04-014	17.5372	−16.853	<5	84 ± 9	27 ± 6	53 ± 1	*nm*
ESO244-G012	19.5356	−44.462	35 ± 3	89 ± 6	24 ± 8	35 ± 2	*m*
CGCG436-030	20.0115	14.362	<7	45 ± 1	72 ± 5	44 ± 1	*em*
ESO353-G020	23.7136	−36.137	22 ± 3	117 ± 6	58 ± 10	87 ± 3	*nm*
RR032-N	24.0975	−37.322	15 ± 2	53 ± 5	19 ± 7	16 ± 1	*m*
RR032-S	24.1006	−37.340	7 ± 3	51 ± 5	16 ± 7	<26	*m*
IRASF01364-1042	24.7205	−10.453	<3	88 ± 5	20 ± 1	28 ± 1	*m*
IIIZw035	26.1271	17.101	<3	30 ± 1	11 ± 1	17 ± 1	*em*
NGC0695	27.8093	22.582	14 ± 2	48 ± 2	18 ± 1	24 ± 1	*nm*
UGC01385	28.7243	36.918	<8	45 ± 5	21 ± 12	48 ± 5	*em*
NGC08380-S	32.428	−10.184	33 ± 4	122 ± 6	31 ± 4	34 ± 2	*em*
NGC0838-E	32.4113	−10.146	22 ± 3	102 ± 5	<16	77 ± 5	*em*
NGC0838-W	32.3530	−10.136	11 ± 3	67 ± 6	<16	58 ± 3	*em*
NGC0828	32.5397	39.190	26 ± 3	111 ± 6	34 ± 10	23 ± 1	*m*
IC0214	33.5232	5.173	7 ± 1	50 ± 1	<3	<8	*m*
NGC0877-N	34.4991	14.544	6 ± 2	21 ± 1	<3	11 ± 1	*m*
NGC0877-S	34.4723	14.521	12 ± 2	27 ± 1	9 ± 1	<9	*m*
MCG+05-06-036-N	35.8416	32.197	<17	86 ± 8	17 ± 3	48 ± 12	*em*
MCG+05-06-036-S	35.8288	32.188	<11	30 ± 8	<13	15 ± 6	*em*
UGC01845	36.0332	47.970	32 ± 3	99 ± 5	29 ± 9	65 ± 3	*nm*
NGC0958	37.6785	−2.939	11 ± 1	21 ± 1	5 ± 1	12 ± 1	*nm*
NGC0992	39.3561	21.101	14 ± 4	54 ± 5	40 ± 5	26 ± 2	*nm*
UGC02238	41.5729	13.096	<16	68 ± 6	54 ± 6	29 ± 1	*m*
IRASF02437+2122	41.6631	21.586	<8	34 ± 1	12 ± 2	<18	*em*
UGC02369	43.5077	14.971	<6	35 ± 6	19 ± 4	37 ± 8	*m*
UGC02608-N	48.7561	42.036	<8	69 ± 6	17 ± 7	50 ± 5	*em*
UGC02608-S	48.8108	41.981	<2	<68	<50	<29	*em*
NGC1275	49.9507	41.512	<11	139 ± 8	99 ± 14	208 ± 3	*nm*
IRASF03217+4022	51.2724	40.559	16 ± 3	54 ± 6	19 ± 9	<29	*nm*
NGC1365	53.4015	−36.140	35 ± 6	196 ± 5	82 ± 9	119 ± 6	*nm*
IRASF03359+1523	54.6964	15.548	13 ± 3	31 ± 1	12 ± 1	<9	*m*
CGCG465-012-N	58.5320	15.990	7 ± 1	20 ± 1	8 ± 1	20 ± 2	*em*
CGCG465-012-S	58.5665	15.929	16 ± 1	45 ± 1	17 ± 2	29 ± 1	*em*
IRAS03582+6012-E	60.6375	60.345	3 ± 1	29 ± 1	16 ± 1	16 ± 1	*m*
IRAS03582+6012-W	60.6332	60.344	4 ± 1	20 ± 1	10 ± 1	6 ± 1	*m*
UGC02982	63.0945	5.547	22 ± 1	67 ± 1	37 ± 2	17 ± 1	*nm*
ESO420-G013	63.4571	−32.007	<8	119 ± 5	54 ± 11	72 ± 4	*nm*
NGC1572	65.6784	−40.601	18 ± 3	97 ± 7	41 ± 9	40 ± 2	*nm*
IRAS04271+3849	67.6379	38.930	24 ± 3	83 ± 6	29 ± 11	51 ± 3	*m*
NGC1614	68.4994	−8.579	<16	130 ± 6	72 ± 11	69 ± 3	*m*
UGC03094	68.8910	19.172	<3	33 ± 6	<14	40 ± 1	*nm*
ESO203-IG001	71.7075	−48.559	<4	29 ± 1	11 ± 2	11 ± 1	*m*
MCG-05-12-006	73.0207	−32.991	<9	50 ± 5	<25	22 ± 2	*nm*
NGC1797	76.9368	−8.019	36 ± 3	57 ± 5	<26	32 ± 3	*em*
CGCG468-002-W	77.0821	17.363	3 ± 2	35 ± 4	12 ± 10	30 ± 6	*em*
CGCG468-002-E	77.0884	17.369	8 ± 3	55 ± 5	28 ± 8	<29	*em*
IRAS05083+2441-S	77.8578	24.755	15 ± 4	44 ± 6	23 ± 11	45 ± 3	*em*
VIIZw031	79.193 3	79.670	<6	51 ± 9	24 ± 4	30 ± 5	*nm*
IRAS05129+5128	79.2332	51.532	<7	47 ± 6	72 ± 19	106 ± 12	*m*
IRASF05189-2524	80.2559	−25.363	<18	38 ± 6	16 ± 1	<34	*m*
IRASF05187-1017	80.2772	−10.246	<4	32 ± 1	18 ± 5	<28	*nm*
IRAS05223+1908	81.3195	19.180	<6	<12	<16	<34	*m*
MCG+08-11-002	85.1821	49.695	40 ± 3	107 ± 6	46 ± 10	53 ± 3	*m*
NGC1961	85.5200	69.379	20 ± 3	169 ± 6	69 ± 5	<32	*m*
UGC03351	86.4501	58.701	29 ± 3	95 ± 6	33 ± 8	31 ± 1	*nm*

Table 2
(Continued)

Name	RA deg	Dec deg	S(0) Flux 10^{-18} Wm^{-2}	S(1) Flux 10^{-18} Wm^{-2}	S(2) Flux 10^{-18} Wm^{-2}	S(3) Flux 10^{-18} Wm^{-2}	Merger stage[a]
IRAS05442+1732	86.7967	17.563	35 ± 3	87 ± 6	44 ± 8	22 ± 2	*em*
IRASF06076-2139	92.4406	−21.674	<8	30 ± 5	12 ± 3	24 ± 7	*m*
UGC03410-E	93.6265	80.450	17 ± 1	68 ± 1	24 ± 1	<8	*m*
UGC03410-W	93.4941	80.477	15 ± 1	30 ± 1	12 ± 2	5 ± 1	*m*
NGC2146	94.6571	78.357	100 ± 9	275 ± 5	<23	122 ± 4	*m*
ESO255-IG007-W	96.8404	−47.177	33 ± 3	79 ± 8	26 ± 3	53 ± 7	*m*
ESO255-IG007-E	96.8440	−47.180	<3	22 ± 4	<54	<26	*m*
ESO255-IG007-S	96.8462	−47.184	10 ± 2	17 ± 16	8 ± 8	<25	*m*
ESO557-G002-N	97.9467	−17.621	<2	51 ± 1	19 ± 1	28 ± 1	*em*
ESO557-G002-S	97.9405	−17.646	<1	15 ± 1	7 ± 1	<8	*em*
UGC03608	104.3934	46.403	27 ± 4	102 ± 5	35 ± 6	51 ± 2	*m*
IRASF06592-6313	104.9177	−63.298	13 ± 3	53 ± 7	19 ± 5	35 ± 2	*nm*
AM0702-601-N	105.8506	−60.256	<4	26 ± 8	72 ± 4	<30	*em*
AM0702-601-S	105.8688	−60.279	10 ± 3	47 ± 7	<13	27 ± 8	*em*
NGC2342	107.3253	20.636	12 ± 3	37 ± 5	20 ± 5	24 ± 1	*em*
NGC2369	109.1607	−62.339	7 ± 1	56 ± 1	36 ± 1	23 ± 1	*nm*
IRAS07251-0248	111.9068	−2.915	<8	13 ± 4	137 ± 3	<28	*m*
NGC2388	112.2227	33.819	<8	89 ± 6	59 ± 12	65 ± 1	*em*
MCG+02-20-003-N	113.9310	11.710	27 ± 3	69 ± 5	23 ± 8	<29	*em*
MCG+02-20-003-S	113.9230	11.612	<2	<22	<13	<8	*em*
IRAS08355-4944	129.2578	−49.908	<9	38 ± 5	<17	<31	*m*
NGC2623	129.6003	25.755	<8	64 ± 6	31 ± 14	51 ± 3	*m*
ESO432-IG006-W	131.1134	−31.697	14 ± 2	46 ± 5	18 ± 8	48 ± 4	*m*
ESO432-IG006-E	131.1205	−31.692	8 ± 2	46 ± 5	28 ± 9	56 ± 5	*m*
ESO60-IG016	133.1336	−69.032	<7	<26	19 ± 4	16 ± 6	*m*
IRASF08572+3915	135.1058	39.065	<9	11 ± 7	<14	<27	*m*
IRAS09022-3615	136.0529	−36.450	<8	107 ± 8	52 ± 5	72 ± 6	*m*
UGC04881-E	138.9796	44.332	7 ± 3	29 ± 2	13 ± 1	24 ± 1	*m*
UGC05101	143.9652	61.353	24 ± 3	42 ± 12	20 ± 3	25 ± 7	*m*
MCG+08-18-013	144.1283	48.469	<2	<4	<2	<8	*em*
Arp303-N	146.5879	3.071	11 ± 1	29 ± 1	10 ± 1	14 ± 1	*em*
Arp303-S	146.5846	3.046	11 ± 1	31 ± 1	12 ± 1	<8	*em*
NGC3110	151.0088	−6.475	15 ± 2	59 ± 7	28 ± 6	45 ± 1	*em*
ESO374-IG032	151.5194	−33.885	<11	40 ± 6	21 ± 4	28 ± 7	*m*
IRASF10173+0828	155.0009	8.226	<3	13 ± 3	<2	<8	*em*
NGC3221	155.5844	21.573	14 ± 1	36 ± 1	18 ± 2	5 ± 1	*m*
NGC3256	156.9636	−43.904	96 ± 15	343 ± 6	149 ± 10	171 ± 3	*m*
ESO264-G036	160.7813	−46.212	9 ± 1	38 ± 1	20 ± 1	22 ± 1	*nm*
ESO264-G057	164.7571	−43.440	21 ± 1	50 ± 1	22 ± 1	<8	*m*
IRASF10565+2448	164.8256	24.543	<7	59 ± 7	22 ± 4	34 ± 6	*m*
MCG+07-23-019	165.9717	40.849	<2	48 ± 1	<2	33 ± 1	*m*
CGCG011-076	170.3011	−2.984	<5	62 ± 1	62 ± 1	50 ± 3	*m*
IRASF11231+1456	171.4377	14.677	12 ± 2	27 ± 2	12 ± 2	21 ± 1	*em*
ESO319-G022	171.9758	−41.614	15 ± 2	42 ± 6	16 ± 8	27 ± 3	*m*
NGC3690-W	172.1291	58.561	<33	150 ± 6	95 ± 8	48 ± 1	*m*
NGC3690-E	172.1402	58.563	166 ± 20	228 ± 5	148 ± 8	<48	*m*
ESO320-G030	178.304	−39.131	4 ± 1	41 ± 1	21 ± 1	46 ± 1	*nm*
ESO440-IG058-S	181.7161	−31.950	21 ± 3	70 ± 5	19 ± 10	36 ± 2	*m*
ESO440-IG058-N	181.7154	−31.946	<3	13 ± 5	<18	<27	*m*
IRASF12112+0305	183.4419	2.812	<3	38 ± 1	14 ± 1	20 ± 1	*m*
NGC4194	183.5402	54.526	<9	98 ± 6	37 ± 17	136 ± 5	*m*
ESO267-G030-E	183.5534	−47.228	21 ± 3	56 ± 5	25 ± 11	21 ± 2	*em*
ESO267-G030-W	183.4678	−47.274	32 ± 3	46 ± 4	15 ± 6	47 ± 4	*em*
IRAS12116-5615	183.592	−56.542	<8	92 ± 7	33 ± 16	<26	*nm*
IRASF12224-0624	186.266	−6.681	<2	6 ± 1	<3	<7	*nm*
UGC08058	194.0595	56.874	<33	57 ± 15	<14	<38	*m*
NGC4922	195.3553	29.314	<8	66 ± 7	32 ± 11	34 ± 1	*m*
CGCG043-099	195.4617	4.333	<4	51 ± 3	24 ± 1	32 ± 1	*m*
MCG-02-33-098-W	195.5819	−15.768	16 ± 3	45 ± 5	35 ± 9	44 ± 3	*m*
MCG-02-33-098-E	195.5849	−15.767	10 ± 3	27 ± 5	<19	<28	*m*
ESO507-G070	195.7184	−23.922	37 ± 4	151 ± 6	87 ± 6	152 ± 4	*m*
IRAS13052-5711	197.0780	−57.458	23 ± 1	73 ± 1	32 ± 1	30 ± 1	*em*
IC0860	198.7647	24.619	<8	42 ± 1	23 ± 1	<8	*nm*
IRAS13120-5453	198.7767	−55.157	<19	87 ± 9	<22	85 ± 8	*m*

Table 2
(Continued)

Name	RA deg	Dec deg	S(0) Flux 10^{-18} Wm^{-2}	S(1) Flux 10^{-18} Wm^{-2}	S(2) Flux 10^{-18} Wm^{-2}	S(3) Flux 10^{-18} Wm^{-2}	Merger stage[a]
VV250a-E	198.8957	62.125	<9	64 ± 8	22 ± 5	43 ± 8	*m*
VV250a-W	198.8779	62.129	<4	<14	<29	<30	*m*
UGC08387	200.1473	34.139	39 ± 4	141 ± 1	58 ± 2	81 ± 1	*m*
NGC5104	200.3462	0.342	14 ± 7	76 ± 7	26 ± 5	51 ± 2	*nm*
MCG-03-34-064	200.6019	−16.728	<9	41 ± 6	<41	<36	*em*
NGC5135	201.4332	−29.833	18 ± 3	121 ± 6	92 ± 8	88 ± 3	*nm*
ESO173-G015	201.8491	−57.489	225 ± 4	333 ± 5	192 ± 104	<31	*nm*
IC4280	203.2225	−24.207	14 ± 1	51 ± 1	18 ± 2	36 ± 1	*nm*
NGC5256	204.5719	48.276	<4	82 ± 2	23 ± 10	38 ± 2	*nm*
Arp240-E	204.9907	0.831	7 ± 5	37 ± 9	<14	12 ± 1	*m*
Arp240-W	204.9708	0.840	14 ± 4	29 ± 8	<15	15 ± 1	*m*
UGC08696	206.1755	55.887	<16	88 ± 10	51 ± 4	100 ± 7	*m*
UGC08739	207.3081	35.257	20 ± 1	59 ± 1	26 ± 2	<8	*nm*
ESO221-IG010	207.7372	−49.055	23 ± 3	70 ± 5	9 ± 9	75 ± 4	*nm*
NGC5331-S	208.0675	2.101	14 ± 1	66 ± 1	15 ± 4	29 ± 1	*m*
NGC5331-N	208.0685	2.109	7 ± 1	28 ± 1	14 ± 1	5 ± 1	*m*
Arp84-S	209.6584	37.424	<3	13 ± 6	<17	<8	*m*
Arp84-N	209.6401	37.454	28 ± 3	72 ± 6	34 ± 6	54 ± 1	*m*
CGCG247-020	214.9302	49.237	<7	48 ± 1	14 ± 4	31 ± 2	*nm*
NGC5653	217.5435	31.215	17 ± 4	63 ± 5	28 ± 10	<29	*nm*
IRASF14348-1447	219.4095	−15.007	10 ± 3	46 ± 1	23 ± 1	28 ± 2	*m*
IRASF14378-3651	220.2454	−37.076	<4	12 ± 9	7 ± 5	18 ± 9	*m*
NGC5734-N	221.2877	−20.870	16 ± 3	58 ± 5	19 ± 7	35 ± 3	*em*
NGC5734-S	221.2959	−20.913	6 ± 3	31 ± 4	15 ± 8	<27	*em*
VV340a-N	224.2529	24.618	14 ± 1	43 ± 1	23 ± 1	20 ± 1	*em*
VV340a-S	224.2513	24.607	3 ± 1	10 ± 1	4 ± 1	<8	*em*
CGCG049-057	228.3076	7.223	3 ± 1	15 ± 1	17 ± 1	12 ± 1	*nm*
ESO099-G004	231.2416	−63.125	33 ± 3	41 ± 5	<17	<30	*m*
IRASF15250+3608	231.7475	35.977	<9	42 ± 13	8 ± 4	<27	*m*
NGC5936	232.5033	12.989	17 ± 3	63 ± 5	72 ± 7	55 ± 3	*nm*
Arp220	233.7385	23.503	<79	174 ± 7	114 ± 10	89 ± 3	*m*
NGC5990	236.5684	2.415	32 ± 3	81 ± 5	32 ± 8	65 ± 2	*em*
NGC6052	241.3036	20.543	18 ± 3	29 ± 4	21 ± 7	19 ± 1	*m*
NGC6090	242.9196	52.457	<5	103 ± 7	155 ± 4	⋯	*m*
IRASF16164-0746	244.7991	−7.901	13 ± 3	98 ± 1	44 ± 2	38 ± 3	*m*
CGCG052-037	247.7356	4.083	<5	61 ± 1	24 ± 2	34 ± 2	*nm*
NGC6156	248.7190	−60.619	36 ± 3	66 ± 5	32 ± 7	38 ± 2	*nm*
ESO069-IG006	249.5494	−68.436	<7	88 ± 13	33 ± 4	39 ± 7	*m*
IRASF16399-0937	250.6671	−9.720	<7	88 ± 7	34 ± 6	56 ± 12	*m*
ESO453-G005-S	251.87895	−29.356	<1	21 ± 1	<6	8 ± 1	*em*
ESO453-G005-N	251.8723	−29.319	4 ± 1	15 ± 1	7 ± 2	<8	*em*
NGC6240	253.2454	2.401	<15	470 ± 8	332 ± 42	672 ± 17	*m*
IRASF16516-0948	253.5988	−9.889	18 ± 1	112 ± 1	39 ± 2	45 ± 1	*m*
NGC6286-S	254.6308	58.936	36 ± 2	63 ± 7	21 ± 6	<8	*m*
IRASF17132+5313	258.5833	53.175	<4	36 ± 2	17 ± 1	18 ± 1	*m*
IRASF17138-1017	259.1483	−10.344	<12	80 ± 7	<25	18 ± 1	*m*
ESO138-G027	261.6806	−59.932	<8	32 ± 5	22 ± 9	32 ± 5	*nm*
UGC11041	268.7159	34.776	15 ± 3	59 ± 5	26 ± 8	30 ± 3	*nm*
CGCG141-034	269.2360	24.017	<8	42 ± 5	12 ± 6	20 ± 2	*nm*
IRAS17578-0400-N	270.1327	−4.015	17 ± 2	63 ± 5	37 ± 7	17 ± 3	*em*
IRAS17578-0400-S	270.1420	−4.029	<3	11 ± 7	72 ± 51	15 ± 4	*em*
IRAS17578-0400-W	270.1012	−4.018	<3	17 ± 5	<16	<31	*em*
IRAS18090+0130-E	272.9101	1.528	19 ± 3	61 ± 6	<18	25 ± 9	*m*
IRAS18090+0130-W	272.8892	1.528	<6	32 ± 5	10 ± 7	<29	*m*
NGC6621	273.2308	68.363	18 ± 3	50 ± 5	27 ± 12	<2	*m*
IC4687	273.4084	−57.725	8 ± 1	126 ± 7	7 ± 2	34 ± 1	*m*
CGCG142-034-E	274.1695	22.113	17 ± 1	60 ± 2	34 ± 7	23 ± 2	*m*
CGCG142-034-W	274.1410	22.111	8 ± 2	24 ± 1	6 ± 1	18 ± 2	*m*
IRASF18293-3413	278.1712	−34.191	50 ± 3	211 ± 6	109 ± 9	102 ± 3	*m*
NGC6670-W	278.3927	59.888	10 ± 1	39 ± 2	12 ± 1	17 ± 1	*m*
NGC6670-E	278.4073	59.890	10 ± 1	38 ± 1	<2	16 ± 1	*m*
IC4734	279.6073	−57.490	24 ± 2	101 ± 5	51 ± 8	69 ± 11	*nm*
NGC6701	280.8022	60.653	25 ± 3	90 ± 5	36 ± 8	<26	*nm*

Table 2
(Continued)

Name	RA deg	Dec deg	S(0) Flux 10^{-18} Wm^{-2}	S(1) Flux 10^{-18} Wm^{-2}	S(2) Flux 10^{-18} Wm^{-2}	S(3) Flux 10^{-18} Wm^{-2}	Merger stage[a]
VV414-W	287.7250	73.410	19 ± 286	36 ± 5	20 ± 17	22 ± 2	*m*
VV414-E	287.7682	73.426	<8	32 ± 6	<15	<31	*m*
ESO593-IG008	288.6298	−21.318	<2	64 ± 2	28 ± 1	26 ± 1	*m*
IRASF19297-0406	293.0885	−3.999	<5	49 ± 4	28 ± 10	31 ± 12	*m*
IRAS19542+1110	299.1491	11.318	<7	<23	14 ± 6	13 ± 8	*nm*
ESO339-G011	299.4067	−37.936	29 ± 3	48 ± 5	35 ± 8	40 ± 3	*nm*
NGC6907	306.2774	−24.809	21 ± 3	85 ± 4	35 ± 10	53 ± 3	*nm*
MCG+04-48-002	307.1461	25.733	18 ± 3	67 ± 7	24 ± 9	<27	*em*
NGC6926	308.2755	−2.027	13 ± 1	32 ± 1	10 ± 1	<8	*m*
IRAS20351+2521	309.3229	25.527	<7	51 ± 6	23 ± 9	29 ± 7	*nm*
CGCG448-020-W	314.3504	17.126	5 ± 3	31 ± 5	<19	<25	*m*
CGCG448-020-E	314.3516	17.128	<8	68 ± 6	29 ± 5	46 ± 7	*m*
IRAS20551-4250	314.6116	−42.650	<11	68 ± 12	32 ± 3	43 ± 6	*m*
ESO286-G035	316.0463	−43.593	12 ± 3	56 ± 5	26 ± 1	30 ± 3	*m*
IRAS21101+5810	317.8720	58.386	<7	37 ± 5	15 ± 4	15 ± 1	*m*
ESO343-IG013-S	324.0439	−38.545	13 ± 1	48 ± 1	22 ± 2	14 ± 1	*m*
ESO343-IG013-N	324.0455	−38.542	26 ± 4	25 ± 1	10 ± 2	25 ± 1	*m*
NGC7130	327.0813	−34.952	<5	69 ± 6	36 ± 8	29 ± 2	*m*
ESO467-G027	333.6665	−27.464	9 ± 1	38 ± 1	13 ± 1	14 ± 1	*nm*
IC5179	334.0446	−36.840	5	18 ± 1	9 ± 1	9 ± 1	*nm*
ESO602-G025	337.8562	−19.035	<16	44 ± 7	88 ± 21	53 ± 3	*nm*
UGC12150	340.3011	34.249	30 ± 3	67 ± 7	25 ± 6	30 ± 1	*nm*
IRASF22491-1808	342.9556	−17.873	<4	16 ± 1	8 ± 1	<7	*m*
NGC7469	345.8151	8.874	<13	162 ± 7	79 ± 11	178 ± 4	*em*
CGCG453-062	346.2355	19.552	<3	51 ± 1	16 ± 2	<29	*nm*
ESO148-IG002	348.9459	−59.055	<5	15 ± 13	<12	<28	*m*
IC5298	349.0029	25.557	<9	38 ± 1	36 ± 2	29 ± 2	*nm*
NGC7552	349.0386	−42.587	<3	100 ± 1	59 ± 1	85 ± 1	*nm*
NGC7591	349.5678	6.586	<8	53 ± 5	72 ± 7	<31	*nm*
NGC7592-E	349.5946	−4.416	<4	35 ± 1	13 ± 1	9 ± 1	*m*
NGC7592-W	349.5912	−4.416	20 ± 3	72 ± 1	25 ± 1	9 ± 1	*m*
ESO077-IG014-E	350.2727	−69.213	10 ± 1	34 ± 2	14 ± 1	15 ± 1	*m*
ESO077-IG014-W	350.2655	−69.217	7 ± 1	34 ± 2	12 ± 1	13 ± 1	*m*
NGC7674	351.9863	8.779	<7	44 ± 2	<3	<12	*em*
NGC7679	352.1943	3.511	<6	66 ± 5	27 ± 8	<14	*em*
IRASF23365+3604	354.7554	36.353	<3	19 ± 11	9 ± 4	24 ± 9	*m*
MCG-01-60-022	355.5038	−3.615	<8	64 ± 5	26 ± 6	107 ± 11	*m*
IRAS23436+5257	356.5226	53.234	12 ± 3	49 ± 7	167 ± 5	45 ± 12	*em*
Arp86-N	356.7705	29.483	5 ± 2	15 ± 1	5 ± 1	<8	*m*
Arp86-S	356.7446	29.459	11 ± 2	32 ± 1	12 ± 1	24 ± 1	*m*

Note.
[a] Stierwalt et al. (2014) give H_2 S(3) fluxes obtained by simultaneously by fitting the dust and gas absorption, emission and continuum gas and dust features. To achieve this Stierwalt et al. (2014) scale the SL spectra to match the LL spectra.
The GOALS sources were classified in 5 stages, Petric et al. (2011); Stierwalt et al. (2013), e.g., Figure 10 in Petric et al. (2011). The merger classifications for each LIRG is given in Stierwalt et al. (2013) and a subset was re-evaluated by Larson et al. (2016). Here we compress the merger stages in three categories, non mergers (*nm*): targets without obvious signs of morphological disturbances, early-mergers (*em*): galaxies are within 1 arcmin of each other but show little or no morphological disturbance, mergers (*m*): this includes all other stages of gravitational interactions.

(This table is available in machine-readable form.)

142-034, NGC 6240, and MCG+04-18-002. The measured S(1) FWHM of these source range between 603 and 781 km s^{-1}, with a median of 653 km s^{-1}, while their S(0) FWHMs range between 611 and 835 km s^{-1}, with a median of 785 km s^{-1}.

3.3. Excitation Diagrams, Masses, and Temperatures of Molecular H_2

Figure 5 presents the excitation diagrams for the sources where we detected at least two of the rotational transitions in the IRS SH, LH, or SL spectra. An excitation diagram is a plot of the column density in the upper level of each transition (N_u), normalized by its statistical weight (g_u) as a function of the temperature T_u associated with the upper level energy E_u. We visually inspect all the excitation diagrams to determine whether more than one temperature component is needed to model the data. For most sources, two temperature fits are not well-constrained, i.e., the masses and temperatures we derive are not the results from a fit. Instead, they are estimates of four unknown parameters from four emission line fluxes; therefore we cannot provide comparisons of χ^2 as a function of the number of temperature components. We are cognizant of the

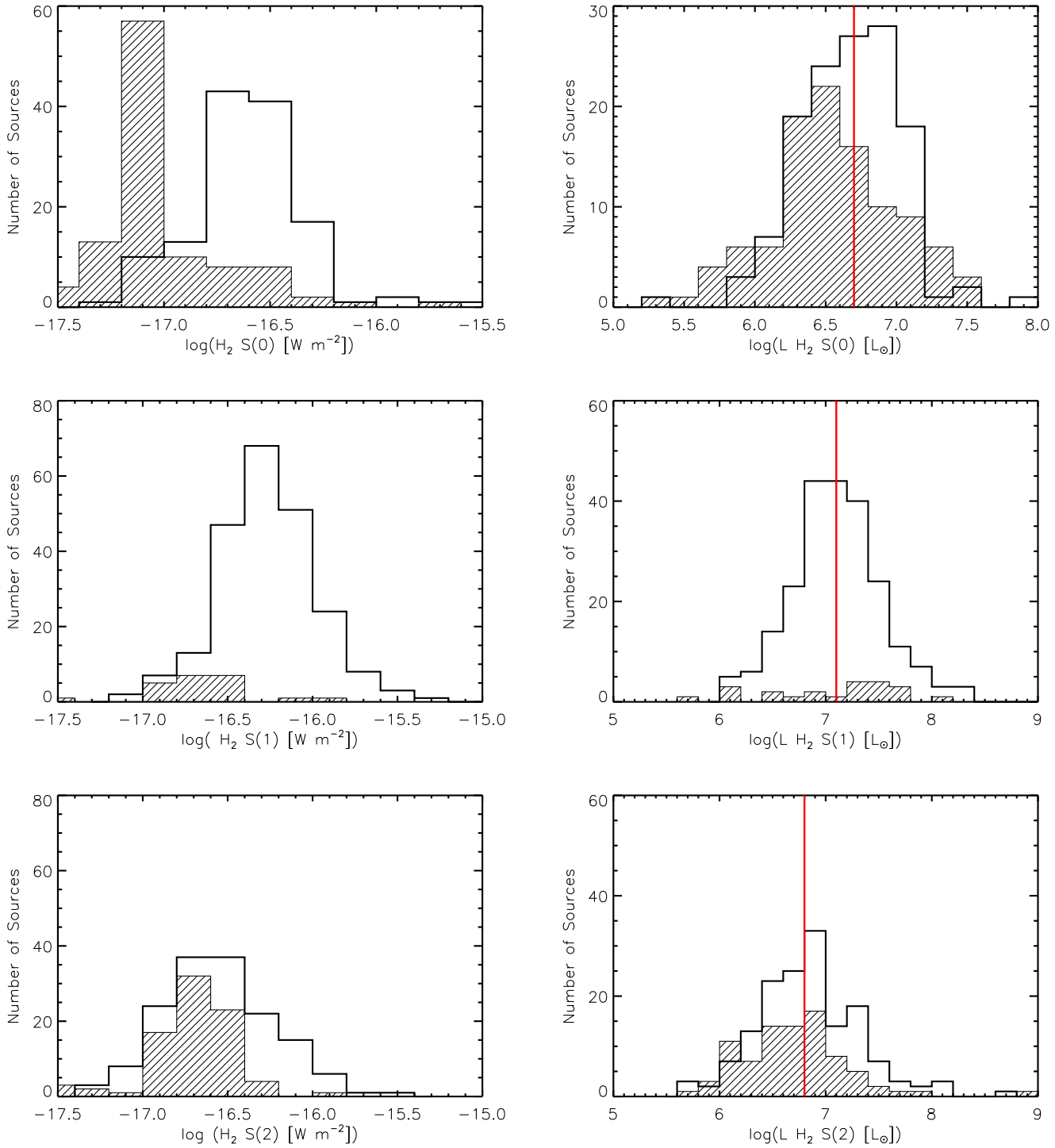

Figure 2. Histograms of measured fluxes (left) and luminosities (right) for the H_2 molecular gas corresponding to the following rotational transitions: S(0) S(1), and S(2). The fluxes are given in log [W/m^{-2}] and the luminosities in log of solar units. Solid histogram present our detections. Dashed histograms show the upper limits, and the red vertical lines indicate the median luminosities.

limitations of this approach, but it allows us to qualitatively and consistently compare with other samples of galaxies analyzed in a similar fashion. There are no obvious systemic errors in this method that would erroneously lead to trends between the warm molecular gas properties and the target's morphologies (mergers versus non-mergers) or AGN contribution to the IR emission from their host galaxy.

Errors on the estimated warm H_2 masses and temperatures come from: (1) measurement errors and (2) the assumption that we can describe the data with a simple distribution of one or two temperature components. When we add the H_2 emission line flux uncertainties in quadrature, we find mass estimates errors on the order of 10%–15%. We assess the second source of error by using three methods to estimate warm H_2 masses and temperatures and comparing the results: (1) we use only the S(1) and S(3) lines, as it was done in Hill & Zakamska (2014); (2) we fit the excitation diagrams with detected lines only; and (3) for excitation diagrams where S(0) is not detected, we use

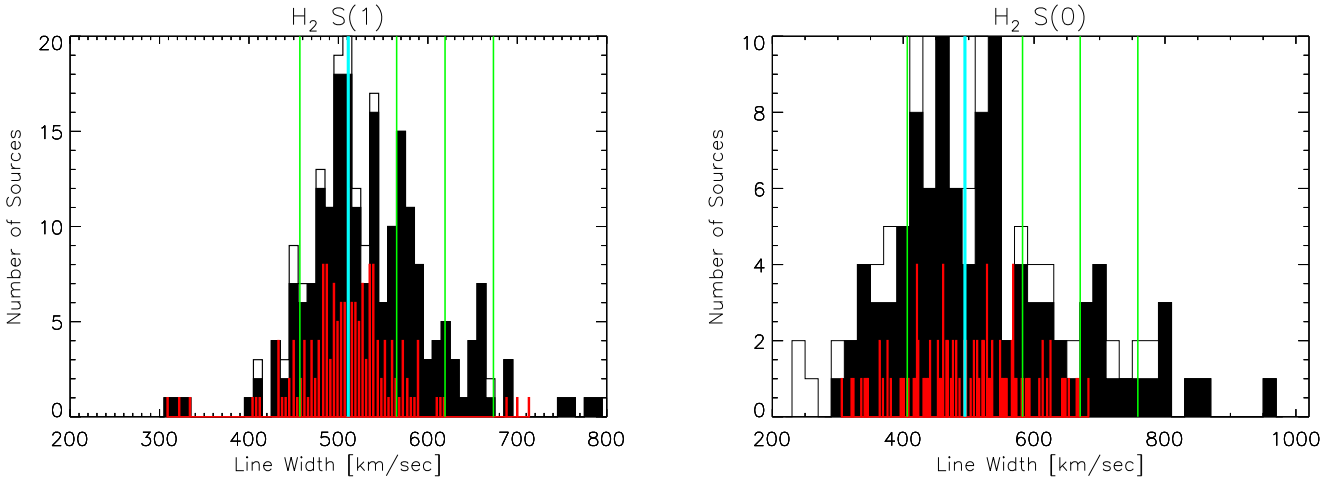

Figure 3. Histograms for H_2 S(1) (left) and H_2 S(0) (right) FWHM measured in the high-resolution IRS modules (using bins of 10 km s^{-1}). In red, we show our model for the distribution of possible measurements if none of the sources were resolved (see text for details). The standard deviation of this distribution, shown in red, is 56 km s^{-1} for the H_2 S(1) transitions. The mode and $\sigma_{\rm inst}$ of the S(0) distribution of FWHMs are 515 and 103 km s^{-1}. The mode is marked in cyan, and the mode + 1, 2, and $3\sigma_{\rm inst}$ and mode—1 × $\sigma_{\rm inst}$ are labeled in green. The black solid histograms show only those widths with errors $\sigma_{\rm FWHM} \leqslant$ FWHM/3.

Table 3
H_2 Detection Statistics from IRS SH and LH Spectra

Line and Units	Detection Rate	Minimum	Maximum	Mean	Median	Standard Dev.
log (S(0)[W m^{-2}])	53%	−17.7	−15.6	−16.5	−16.6	0.5
log ($L_{\rm S(0)}$)[$L_\odot$])	···	5.8	7.9	6.8	6.7	0.8
log (S(1)[W m^{-2}])	91%	−17.2	−15.4	−16.2	−16.3	0.4
log ($L_{\rm S(1)}$ [$L_\odot$])	···	6.0	8.3	7.3	7.1	0.9
log (S(2)[W m^{-2}])	68%	−16.4	−15.5	−16.5	−16.6	0.3
log ($L_{\rm S(2)}$[$L_\odot$])	···	5.7	8.7	7.1	6.8	1.2
log (S(3)[W m^{-2}])	72%	−16.1	−15.2	−16.4	−16.5	0.8
log ($L_{\rm S(3)}$[$L_\odot$]	···	5.2	8.1	7.2	6.9	0.6

the S(0) upper limits as if they were detections and derive an upper limit on the total mass. We find that adding the S(0) line to the excitation diagram fit has the largest impact: the estimated masses become 1.5 larger when we include S(0) measurements. Because LL data often lack the sensitivity to detect the S(0) line, estimates of warm molecular gas masses based on lower-resolution IRS data may be systematically lower than the true values (Roussel et al. 2007; Hill & Zakamska 2014).

To compute warm molecular gas masses and temperatures, we use the same method as Ogle et al. (2010), Higdon et al. (2006), and Roussel et al. (2007). We assume that the gas is in local thermodynamic equilibrium (LTE). The relation between the observed transitions of the H_2 rotational levels and the total column density $N_{\rm TOT}$ are given by:

$$N_u = g_u\, N_{\rm TOT}\, \exp[-E_u/(kT)]/Z(T), \quad (1)$$

where $Z(T)$ is the partition function for the Jth state given by

$$Z(T) = \sum_J \exp(-E_J/kT.) \quad (2)$$

$$T = \frac{E_{u2} - E_{u1}}{k \times \ln(N_{u1}/N_{u2} \times g_{u2}/g_{u1})}, \quad (3)$$

where N_u is the column density in the upper level of each transition, g_u its statistical weight, and E_u its energy. The E_u/k associated with S(0), S(1), S(2), and S(3), as well as the statistical weights for the lines are given in Table 1. The column density N_u is related to the measured flux F emitted in a transition:

$$N_u = \frac{F}{h\nu A} \times \frac{4\pi}{\Omega}, \quad (4)$$

where A is the Einstein coefficient giving the probability for spontaneous emission, $h\nu$ is the transition energy, and Ω is the beam solid angle. The statistical weight is a function of the rotational number J, and the spin number I, given by:

$$g_u = (2I + 1)(2J + 1). \quad (5)$$

The mass can be determined from $N_{\rm TOT}$ with the source size derived from the size of the spectral extraction region: $4\farcs7 \times 4\farcs7$ at the distance of each source (e.g., 2 kpc for a source at a redshift of 0.02).

We estimate that the molecular H_2 gas has mass-averaged effective temperatures between 92 and 650 K, and the sums of the individual mass components are between 10^6 and $10^9\, M_\odot$. The derived values are estimates because the gas may have a distribution of temperatures and also may originate from regions with different physical properties within the few kpc region probed by our spectra. However, such estimates are useful because they provide comparisons with similar analyses done on normal galaxies and ULIRGs. This analysis provides a practical way to characterize the true underlying gas temperatures. With the exception of two

Table 4
General Properties of Galaxies where the H_2 S(1) is Resolved or Marginally Resolved

Name	S(1) FWHM (km s^{-1})	S(1) FWHM Intrinsic (km s^{-1})	[Ne V] Detection Flag [1 detected]	[O IV] Detection Flag [0 not detected]
ESO 353-G020	608	329 ± 46	0	1
IRAS F01364-1042I	1318	1215 ± 173	0	0
IIZw35	658	413 ± 59	0	0
NGC 0828	661	420 ± 59	0	1
MCG+08-11-002	641	386 ± 55	0	1
NGC 1961	624	358 ± 48	0	0
UGC 03351	661	420 ± 52	0	1
ESO 255-IG007	690	464 ± 92	0	0
NGC 2369	583	281 ± 35	0	1
ESO 320-G030	583	281 ± 35	0	0
ESO 507-G070	629	365 ± 45	0	0
IRAS 13052-5711	603	321 ± 40	0	0
VV250a	814	634 ± 126	0	0
IC 4280	620	352 ± 43	0	1
NGC 5256	649	400 ± 44	1	1
NGC 5257_8	782	592 ± 73	0	0
NGC 5331	616	343 ± 43	0	1
NGC 5331	661	420 ± 47	0	0
IRAS F16164-0746	612	336 ± 37	0	1
ESO 069-IG006	752	552 ± 61	0	0
IRAS F16399-0937	661	420 ± 60	0	1
NGC 6240	756	558 ± 56	1	1
CGCG 142-034	653	407 ± 51	0	0
CGCG 142-034	608	329 ± 41	1	1
ESO 593-IG008	690	464 ± 52	0	1
MCG+04-48-002	653	407 ± 68	1	0
NGC 7771	690	464 ± 58	0	1

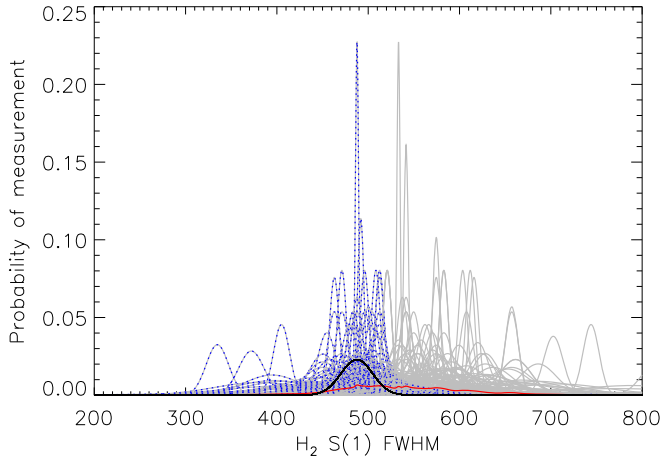

Figure 4. The distribution of derived H_2 line FWHMs (obtained from fitting each line with a Gaussian), each represented as a (gray) Gaussian centered on the measured H_2 line width and a width equal to the estimated error on the measured H_2 line width; the peak of each Gaussian is set to normalize its area to 1. Adding up all the individual Gaussian distributions gives gives the most probable line width measurement for the LIRGs in our sample and is represented as the red, solid curve. The black, solid Gaussian gives the probability distribution of possible measurements of H_2 line width for an unresolved source and was obtained by adding up all the probability distributions for the 94 unresolved sources shown as blue, dotted Gaussian curves. We used this probability distribution and the error on each measurement to compute the likelihood a source is unresolved. The derived estimates that appear lower than the instrumental resolution are sources with poor sampling and/or low signal-to-noise ratio. We keep them here because they indicate the error budget in our measurements.

sources for which we find the coldest temperatures at 92 and 97 K, the coldest components are above 100 K. The LIRGs IRAS 19542+1110 and ESO 339-G011 are the only two sources with total warm molecular gas masses greater than $1 \times 10^9 M_\odot$.

The estimated masses and temperatures of the warm molecular gas emitting in the MIR are presented in Table 5. The median temperature for sources that are fit well by one temperature component is ∼300 K. The median of the total masses is $\log M_\odot = 7.2 \pm 0.5$. Figure 6 shows the distribution of total gas masses normalized by L_{IR} and temperatures (mass-averaged temperatures for sources where we required at least two temperatures to fit the observed rotational lines) as a function of merger stage.

Out of the 214 nuclei for which we determine excitation diagrams, 103 require two temperature components. The average masses of warm molecular gas for objects in the non-interacting (n), early mergers (em), and late-stage mergers (m) are 8.3, 8.9, and $12.5 \times 10^7 M_\odot$, respectively. The average temperatures of warm molecular gas we derive for sources in each of these respective interaction stages are 242, 243, and 277 K respectively.

3.4. Ortho-to-para Ratios

To understand the impact that AGN and gravitational interactions have on the warm molecular gas, we also look at the relative strengths of emission from states with odd total angular momentum to emission from states with even angular momentum, i.e., ortho-to-para ratios (see Appendix B). The H_2 molecule consists of two covalently bound hydrogen atoms. Because its center of mass is the same as that of its electrical charges, it does not have a permanent dipole moment. Therefore, H_2 cannot transition from its ortho state (i.e., odd total angular momentum number J) to its para state (i.e., even J). The value of

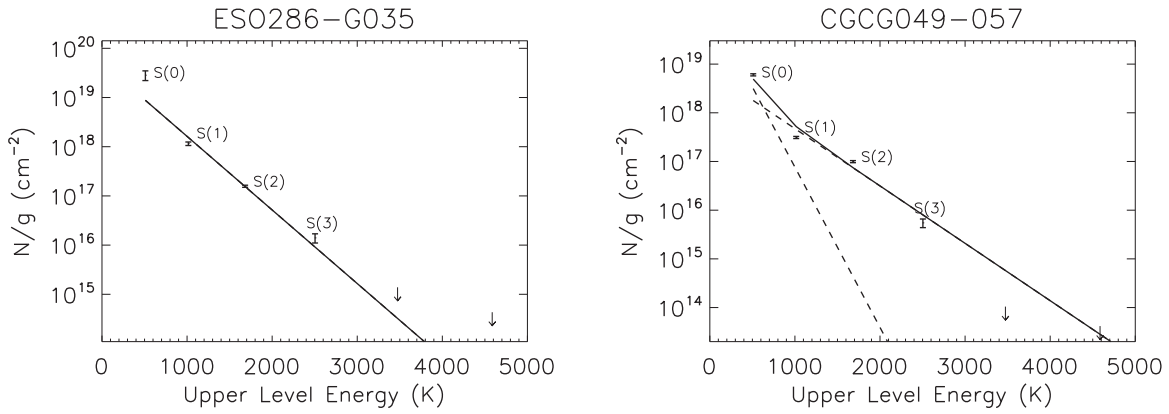

Figure 5. Excitation diagrams. The electronic version contains all the excitation diagrams. Here, we only show two examples of sources well fit by one and two temperature components.

(The complete figure set (214 images) is available.)

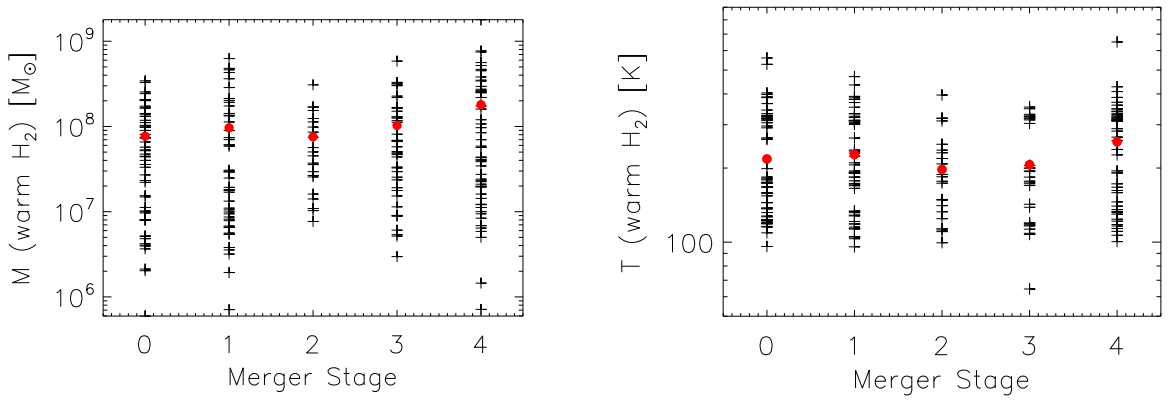

Figure 6. H_2 masses normalized by the L_{IR} (left) and temperatures (right) vs. merger stage. Filled circles use S(0) detections; empty circles use S(0) upper limits. Red circles give the average value for each merger state.

the OPR is related to the history of the molecular cloud. If the gas is in LTE, a Boltzman distribution describes the populations at each energy level, and the OPR is a known function of temperature. At typical 300 K temperatures, the OPR is 3. Measuring OPRs that are lower than 3 may suggest that the gas is not in LTE or that the gas is thermalized at a temperature lower than 300 K (see Flagey et al. (2013) for a similar discussion about H_2O OPR). The thermalization time for H_2 is on the order of 5000 years, so the OPR traces the temperature of the matter with which the H_2 has last thermalized beyond that time. Other interpretations for measuring OPRs that are different than 3 are related to extinction and/or the presences of multiple components along the line of sight (Roussel et al. 2007; Flagey et al. 2013, and references within). Following Roussel et al. (2007), we first determined which sources have non-LTE OPRs using the apparent excitation temperatures derived from the S(0), S(1), S(2), and S(3) lines. More details about how the OPRs were estimated are provided in Appendix A, and Figure 7 shows several illustrative examples.

We find 30 LIRGs with OPR values that appear incompatible with LTE conditions. Among these sources are Arp 220, NGC 3690, and NGC 0992. To test if we observe OPRs incompatible with LTE because of dust, we assume that the amount of extinction is proportional to the silicate strength measured by Stierwalt et al. (2013) using the method described in Spoon et al. (2007). The silicate strength at 9.7 μm is defined as $\log(f_{9.7\,\mu m}/C_{9.7\,\mu m})$, where $f_{9.7\,\mu m}$ is the flux measured at 9.7 μm and $C_{9.7\,\mu m}$ is the continuum flux in the absence of the absorption feature (Spoon et al. 2007; Stierwalt et al. 2013). The silicates strength of Arp 220 is one of the highest in the GOALS sample. NGC 3690 has a silicate strength of -1.65 ± 0.02, which is relatively high for LIRGs, though not one of the highest (Stierwalt et al. 2013). Extinction might be the reason why we observe an OPR incompatible with LTE in those two LIRGs. NGC 0992, however, does not appear to be heavily obscured: Stierwalt et al. (2013) report a silicate strength of 0.05 ± 0.04 for this source. It thus seems that, at least in the case of NGC 0992, either the silicate absorption does not originate in the same region as the warm H_2 or —as is the case for several normal galaxies—the gas is not yet thermalized (Roussel et al. 2007). This could mean (1) that we are observing this galaxy at a peculiar moment in its evolution, which would be surprising given the low critical densities of H_2 rotational transitions, or (2) that, given the large size of our beam, we are recovering emission from regions with heterogeneous physical conditions, with gas at different temperatures.

3.5. H_2 Excitation Conditions

We seek to determine whether the detected warm H_2 gas is emitted primarily in photon-dominated regions (PDRs). MIR rotational lines are rapidly thermalized and hence provide few diagnostics with which to determine the excitation

Table 5
Masses and Temperatures of Warm Molecular Gas as Estimated from MIR Spectroscopy

Source	RA deg	Dec deg	T 1 [K]	log(M1) log($M_\odot$)	T 2 [K]	log(M2) log($M_\odot$)	$\langle T \rangle$ [K]	$\sum M$ log($M_\odot$)
NGC0023	2.470	25.924	113	7.973	386	6.548	123	7.989
NGC0034	2.780	−12.108	124	8.396	318	7.025	132	8.415
MCG-02-01-051	4.710	−10.359	121	8.318	411	6.729	129	8.328
ESO350-IG038	9.220	−33.555	391	6.580	⋯	⋯	391	6.580
NGC0232 - W	10.690	−23.561	116	8.766	517	5.962	116	8.767
NGC0232 - E	10.720	−23.541	175	8.111	11	7.398	148	8.188
MCG+12-02-001	13.520	73.085	193	8.474	15	7.699	167	8.543
NGC0317B	14.420	43.792	324	7.431	⋯	⋯	324	7.431
IC1623AB	16.950	−17.507	528	6.815	⋯	⋯	528	6.815
MCG-03-04-014	17.540	−16.853	115	8.199	359	6.722	122	8.215
ESO244-G012	19.530	−44.462	147	7.870	459	5.652	149	7.873
CGCG436-030	20.010	14.362	211	8.009	464	7.013	234	8.049
ESO353-G020	23.710	−36.137	312	6.831	⋯	⋯	312	6.831
ESO297-G011-N	24.100	−37.322	113	8.497	310	7.146	122	8.516
ESO297-G011-S	24.100	−37.341	365	6.551	⋯	⋯	365	6.551
IRASF01364-1042	24.720	−10.453	169	7.422	308	6.501	184	7.470
IRASF01417+1651	26.130	17.103	223	7.258	⋯	⋯	223	7.258
NGC0695	27.810	22.582	237	7.124	⋯	⋯	237	7.124
UGC01385	28.760	36.920	257	7.193	111	8.307	122	8.340
NGC0838-S	32.430	−10.184	205	7.670	⋯	⋯	205	7.670
NGC0838-E	32.410	−10.146	188	6.885	⋯	⋯	188	6.885
NGC0838-W	32.350	−10.136	174	7.149	⋯	⋯	174	7.149
NGC0828	32.540	39.190	321	7.021	⋯	⋯	321	7.021
IC0214	33.520	5.173	200	7.669	⋯	⋯	200	7.669
NGC0877	34.500	14.544	107	7.692	330	6.441	119	7.716
MCG+05-06-036-N	35.840	32.197	339	6.975	⋯	⋯	339	6.975
MCG+05-06-036-S	35.830	32.188	306	6.749	⋯	⋯	306	6.749
UGC01845	36.030	47.970	348	6.956	⋯	⋯	348	6.956
NGC0958	37.680	−2.939	354	6.473	⋯	⋯	354	6.473
NGC0992	39.360	21.101	333	6.975	⋯	⋯	333	6.975
UGC02238	41.570	13.096	206	7.292	704	6.400	263	7.344
IRASF02437+2122	41.660	21.586	179	7.818	⋯	⋯	179	7.818
UGC02369-2	43.510	14.971	195	8.079	⋯	⋯	195	8.079
UGC02369-1	43.510	14.977	111	8.149	436	5.938	113	8.152
UGC02608-S	48.810	41.981	112	7.655	352	6.745	139	7.706
IRASF03217+4022	51.270	40.559	151	7.845	366	6.436	159	7.862
NGC1365	53.400	−36.141	319	6.683	⋯	⋯	319	6.683
IRASF03359+1523	54.700	15.548	131	8.090	323	6.944	145	8.117
CGCG465-012-N	58.530	15.990	158	7.718	334	6.740	175	7.761
CGCG465-012-S	58.570	15.929	320	7.000	⋯	⋯	320	7.000
IRAS03582+6012-E	60.640	60.345	398	6.623	⋯	⋯	398	6.623
IRAS03582+6012-W	60.630	60.344	310	7.367	⋯	⋯	310	7.367
UGC02982	63.090	5.547	316	6.708	⋯	⋯	316	6.708
ESO420-G013	63.460	−32.007	190	7.780	⋯	⋯	190	7.780
NGC1572	65.680	−40.601	96	8.029	314	7.004	115	8.068
IRAS04271+3849	67.640	38.930	327	7.676	⋯	⋯	327	7.676
NGC1614	68.500	−8.580	386	7.009	⋯	⋯	386	7.009
UGC03094	68.890	19.172	313	7.352	⋯	⋯	313	7.352
ESO203-IG001	71.710	−48.558	316	6.905	⋯	⋯	316	6.905
NGC1797	76.940	−8.019	330	6.910	104	8.869	107	8.873
CGCG468-002-W	77.080	17.363	160	7.604	305	6.651	175	7.650
CGCG468-002-E	77.090	17.369	210	7.761	24	7.207	169	7.868
IRAS05083+2441	77.860	24.755	329	7.086	⋯	⋯	329	7.086
IRASF05081+7936	79.190	79.670	281	6.238	102	8.127	105	8.130
IRAS05129+5128	79.230	51.532	314	5.853	⋯	⋯	314	5.853
IRASF05189-2524	80.260	−25.363	219	8.371	133	7.977	195	8.517
MCG+08-11-002	85.180	49.695	311	6.822	⋯	⋯	311	6.822
NGC1961	85.520	69.379	313	6.286	⋯	⋯	313	6.286
UGC03351	86.450	58.701	111	8.660	329	7.013	115	8.670
IRAS05442+1732	86.800	17.563	111	8.288	331	6.857	119	8.303
IRASF06076-2139	92.440	−21.673	230	7.951	⋯	⋯	230	7.951
UGC03410-E	93.620	80.450	136	7.450	344	6.704	168	7.521

Table 5
(Continued)

Source	RA deg	Dec deg	T 1 [K]	log(M1) log($M_\odot$)	T 2 [K]	log(M2) log($M_\odot$)	$\langle T \rangle$ [K]	$\sum M$ log($M_\odot$)
UGC03410-W	93.490	80.476	650	7.926	⋯	⋯	650	7.926
NGC2146	94.660	78.357	332	6.732	⋯	⋯	332	6.732
ESO255-IG007-W	96.840	−47.177	171	7.786	⋯	⋯	171	7.786
ESO255-IG007-S	96.842	−47.184	200	8.01	⋯	⋯	200	8.01
ESO557-G002-N	97.950	−17.621	347	6.808	⋯	⋯	347	6.808
ESO557-G002-S	97.940	−17.646	111	8.220	422	6.207	113	8.225
UGC03608	104.390	46.403	109	7.629	382	6.415	125	7.655
IRASF06592-6313	104.920	−63.298	470	6.730	⋯	⋯	470	6.730
IRASF07027-6011-1	105.8688	−60.256	350	7.605	⋯	⋯	350	7.605
IRASF07027-6011-2	105.870	−60.279	206	8.400	625	7.330	238	8.436
NGC2342	107.330	20.636	123	8.538	327	7.258	133	8.560
NGC2369	109.160	−62.343	97	8.456	318	7.188	109	8.479
IRAS07251-0248	111.910	−2.915	221	8.350	148	8.196	191	8.581
NGC2388	112.220	33.819	128	8.045	346	6.299	132	8.053
MCG+02-20-003-N	113.930	11.710	113	8.230	364	6.574	118	8.241
IRAS08355-4944	129.2578	−49.908	178	7.73	⋯	⋯	178	7.73
NGC2623	129.600	25.755	96	8.740	310	7.064	101	8.750
ESO432-IG006-W	131.110	−31.697	112	8.013	299	6.933	127	8.045
ESO432-IG006-E	131.120	−31.692	191	7.769	⋯	⋯	191	7.769
ESO60-IG16	133.130	−69.033	319	7.281	⋯	⋯	319	7.281
IRASF08572+3915	135.110	39.065	396	7.037	⋯	⋯	396	7.037
IRAS09022-3615	136.050	−36.450	100	8.790	335	6.931	103	8.797
IRASF09111-1007	138.400	−10.325	135	7.983	463	5.834	138	7.986
UGC04881	138.980	44.333	127	6.816	344	6.170	167	6.904
UGC05101	143.965	61.353	148	8.196	220	8.35	191	8.6
IRASF09437+0317	146.590	3.071	130	8.274	345	6.560	134	8.283
IC0563	146.580	3.046	121	8.633	659	5.699	121	8.633
NGC3110	151.010	−6.475	261	7.554	⋯	⋯	261	7.554
NGC3221	155.580	21.570	322	7.083	⋯	⋯	322	7.083
NGC3256	156.960	−43.904	322	7.382	⋯	⋯	322	7.382
ESO264-G036	160.780	−46.212	105	8.336	401	6.320	107	8.340
ESO264-G057	164.760	−43.440	170	7.373	⋯	⋯	170	7.373
IRASF10565+2448	164.830	24.543	133	8.456	516	6.980	146	8.470
MCG+07-23-019	165.970	40.850	126	8.442	328	6.979	133	8.456
CGCG011-076	170.280	−2.994	258	6.276	677	5.375	306	6.326
ESO319-G022	171.9758	−41.6144	135	7.98	463	5.84	198	7.99
IC2810	171.440	14.677	340	7.438	⋯	⋯	340	7.438
NGC3690-W	172.130	58.561	127	8.636	335	7.260	136	8.654
NGC3690-E	172.140	58.563	109	8.201	341	6.851	119	8.220
ESO320-G030	178.304	−39.131	126	6.8	344	6.17	272	6.9
ESO440-IG058	181.720	−31.946	112	7.723	369	6.639	132	7.757
IRASF12112+0305	183.440	2.812	158	8.072	⋯	⋯	158	8.072
NGC4194	183.540	54.527	303	6.690	117	8.137	124	8.152
ESO267-G030-E	183.550	−47.228	313	7.299	⋯	⋯	313	7.299
ESO267-G030-W	183.470	−47.274	283	7.049	⋯	⋯	283	7.049
IRAS12116-5615	183.590	−56.542	250	7.425	⋯	⋯	250	7.425
IRASF12224-0624	186.270	−6.681	237	7.701	⋯	⋯	237	7.701
NGC4418	186.730	−0.878	348	7.587	⋯	⋯	348	7.587
Mrk231	194.060	56.874	106	8.230	343	6.489	111	8.238
NGC4922	195.360	29.314	247	7.675	124	8.436	143	8.505
MCG-02-33-098	195.580	−15.768	131	8.093	825	5.305	133	8.093
ESO507-G070	195.720	−23.922	184	7.365	⋯	⋯	184	7.365
IRAS13052-5711	197.080	−57.458	103	9.228	329	8.004	116	9.253
IC0860	198.760	24.619	404	7.155	⋯	⋯	404	7.155
IRAS13120-5453	198.780	−55.156	110	8.114	353	6.352	113	8.124
VV250a-E	198.880	62.129	112	8.666	314	7.220	119	8.681
UGC08387	200.150	34.140	184	7.467	⋯	⋯	184	7.467
NGC5104	200.350	0.343	132	6.849	369	5.946	158	6.901
MCG-03-34-064	200.580	−16.708	159	8.398	⋯	⋯	159	8.398
NGC5135	201.430	−29.833	289	7.639	⋯	⋯	289	7.639
ESO173-G015	201.850	−57.489	92	8.400	402	6.480	96	8.405
IC4280	203.220	−24.207	228	7.509	729	6.322	258	7.537

Table 5
(Continued)

Source	RA deg	Dec deg	T 1 [K]	log(M1) log($M_\odot$)	T 2 [K]	log(M2) log($M_\odot$)	$\langle T \rangle$ [K]	$\sum M$ log($M_\odot$)
NGC5256-1	204.570	48.276	121	8.303	444	6.097	123	8.305
NGC5256-2	204.570	48.278	116	8.220	390	6.049	117	8.223
Arp240-E	204.990	0.831	428	7.614	⋯	⋯	428	7.614
Arp240-W	204.970	0.841	112	8.356	322	7.332	130	8.396
Mrk273	206.180	55.887	317	7.049	⋯	⋯	317	7.049
UGC08739	207.310	35.257	121	7.993	378	5.953	124	7.997
ESO221-IG010	207.740	−49.055	311	7.752	⋯	⋯	311	7.752
NGC5331-S	208.070	2.101	316	7.322	⋯	⋯	316	7.322
NGC5331-N	208.070	2.109	311	6.502	⋯	⋯	311	6.502
NGC5395	209.660	37.424	177	7.228	⋯	⋯	177	7.228
NGC5394	209.640	37.454	200	8.398	863	7.009	226	8.415
CGCG247-020	214.930	49.237	157	7.942	293	7.294	182	8.029
NGC5653	217.540	31.215	177	8.053	⋯	⋯	177	8.053
IRASF14348-1447	219.410	−15.007	323	7.470	⋯	⋯	323	7.470
IRASF14378-3651	220.250	−37.076	291	6.924	⋯	⋯	291	6.924
NGC5734-N	221.290	−20.870	329	7.754	⋯	⋯	329	7.754
NGC5734-S	221.300	−20.913	344	6.597	⋯	⋯	344	6.597
VV340a-N	224.250	24.618	130	7.943	369	6.360	137	7.954
VV340a-S	224.250	24.607	320	6.716	⋯	⋯	320	6.716
CGCG049-057	228.3076	7.223	132	6.85	369	5.95	158	6.9
ESO099-G004	231.240	−63.125	173	7.823	⋯	⋯	173	7.823
IRASF15250+3608	231.750	35.977	206	7.303	320	6.741	231	7.408
NGC5936	232.500	12.989	327	6.702	107	8.481	110	8.489
Arp220	233.740	23.503	96	8.225	327	6.360	99	8.230
NGC5990	236.570	2.415	122	8.705	367	7.104	128	8.715
NGC6052	241.300	20.543	165	7.810	358	6.571	175	7.834
NGC6090	242.920	52.458	193	7.838	⋯	⋯	193	7.838
IRASF16164-0746	244.800	−7.901	116	8.303	347	6.747	122	8.316
CGCG052-037	247.740	4.083	180	7.602	⋯	⋯	180	7.602
ESO069-IG006	249.560	−68.455	200	8.093	500	7.555	267	8.204
IRASF16399-0937	250.670	−9.720	560	6.563	⋯	⋯	560	6.563
ESO453-G005-S	251.880	−29.356	116	8.533	430	6.265	118	8.535
ESO453-G005-N	251.870	−29.319	111	8.009	362	6.243	116	8.013
NGC6240	253.250	2.401	184	7.487	⋯	⋯	184	7.487
IRASF16516-0948	253.600	−9.889	175	7.637	⋯	⋯	175	7.637
NGC6286	254.630	58.937	333	7.173	⋯	⋯	333	7.173
IRASF17132+5313	258.590	53.175	323	7.405	⋯	⋯	323	7.405
IRASF17138-1017	259.150	−10.345	325	7.602	⋯	⋯	325	7.602
IRASF17207-0014	260.840	−0.284	15	7.820	290	6.916	46	7.871
ESO138-G027	261.680	−59.932	313	7.207	⋯	⋯	313	7.207
UGC11041	268.720	34.776	111	8.093	302	6.732	120	8.111
CGCG141-034	269.240	24.017	111	8.173	387	6.076	113	8.179
IRAS17578-0400-N	270.130	−4.015	317	6.699	⋯	⋯	317	6.699
IRAS17578-0400-S	270.140	−4.029	133	7.612	296	6.511	145	7.644
IRAS17578-0400-W	270.100	−4.018	111	7.167	309	5.858	120	7.188
IRAS18090+0130-E	272.910	1.528	380	6.899	⋯	⋯	380	6.899
IRAS18090+0130-W	272.890	1.528	135	8.382	404	6.322	137	8.386
NGC6621	273.230	68.363	360	7.294	⋯	⋯	360	7.294
IC4687	273.420	−57.725	296	6.999	⋯	⋯	296	6.999
CGCG142-034-E	274.170	22.113	341	5.775	⋯	⋯	341	5.775
CGCG142-034-W	274.140	22.111	389	6.607	⋯	⋯	389	6.607
IRASF18293-3413	278.170	−34.191	304	6.783	⋯	⋯	304	6.783
NGC6670-W	278.390	59.888	109	8.467	287	7.143	117	8.487
NGC6670-E	278.410	59.890	149	8.210	328	7.100	162	8.241
IC4734	279.610	−57.490	115	8.513	303	7.201	124	8.534
VV414-W	287.730	73.410	311	6.740	⋯	⋯	311	6.740
VV414-E (NGC6786)	287.770	73.426	370	6.769	⋯	⋯	370	6.769
ESO593-IG008	288.630	−21.318	353	6.938	⋯	⋯	353	6.938
IRASF19297-0406	293.090	−4.000	106	8.380	510	7.344	140	8.418
IRAS19542+1110	299.150	11.318	192	6.931	⋯	⋯	192	6.931
ESO339-G011	299.410	−37.936	108	7.924	325	6.246	112	7.933
NGC6907	306.280	−24.809	191	7.258	⋯	⋯	191	7.258

Table 5
(Continued)

Source	RA deg	Dec deg	T 1 [K]	log(M1) log($M_\odot$)	T 2 [K]	log(M2) log($M_\odot$)	$\langle T \rangle$ [K]	$\sum M$ log($M_\odot$)
MCG+04-48-002	307.150	25.733	132	7.974	338	6.633	141	7.993
NGC6926	308.280	−2.027	325	7.057	⋯	⋯	325	7.057
IRAS20351+2521	309.324	25.527	334	7.167	⋯	⋯	334	7.167
CGCG448-020-W	314.350	17.126	200	7.688	⋯	...	200	7.688
CGCG448-020-E	314.352	17.128	250	7.871	⋯	⋯	250	7.871
ESO286-G035	316.046	−43.593	319	6.712	⋯	⋯	319	6.712
ESO343-IG013-S	324.044	−38.545	111	8.093	302	8.09	294	8.110
ESO343-IG013-N	324.046	−38.542	121	8.204	694	5.34	394	8.207
NGC7130	327.081	−34.952	317	6.7	⋯	⋯	317	6.7
ESO467-G027	333.666	−27.464	133	7.611	296	6.51	256	7.644
IC5179	334.045	−36.840	110	7.167	308	5.86	120	7.187
ESO602-G025	337.856	−19.035	379	6.899	⋯	⋯	379	6.899
UGC12150	340.301	34.249	135	8.38	404	6.32	137	8.39
IRASF22491-1808	342.956	−17.873	313	7.513	⋯	⋯	313	7.513
NGC7469	345.815	8.874	369	6.912	⋯	⋯	369	6.912
CGCG453-062	346.236	19.552	296	6.99	⋯	⋯	296	6.99
IC5298	349.003	25.557	387	6.835	⋯	⋯	387	6.835
NGC7552	349.039	−42.587	340	5.77	⋯	⋯	340	5.77
NGC7591	349.568	6.586	381	6.61	⋯	⋯	381	6.61
NGC7592-E	349.595	−4.416	303	6.783	⋯	⋯	303	6.783
NGC7592-W	349.591	−4.416	110	8.467	287	7.14	117	8.487
ESO077-IG014-E	350.273	−69.213	148	8.21	328	7.1	162	8.24
ESO077-IG014-W	350.265	−69.217	115	8.51	304	7.2	124	8.53
NGC7679	352.194	3.511	310	6.739	⋯	⋯	310	6.739
IRASF23365+3604	354.755	36.353	370	6.769	⋯	⋯	370	6.769
MCG-01-60-022	355.504	−3.615	353	6.93	⋯	⋯	353	6.93
Arp86-N	356.771	29.483	192	6.94	⋯	⋯	192	6.94
Arp86-S	356.745	29.459	108	7.92	325	6.24	112	7.93

(This table is available in machine-readable form.)

mechanisms. However, some conjectures can be made by comparing the emission of the warm H_2 gas to that from other MIR coolants known to originate in PDRs, such as [Si II] and PAH emission (Kaufman et al. 2006; Cluver et al. 2010).

About 80% of the LIRGs nuclei in GOALS have MIR colors (using continuum fluxes measured in the IRAC 3.6, 4.5, 5.8, and 8 μm bands, as well as 15/5.5 μm fluxes) that are consistent with a PDR origin for the observed MIR dust continuum (Petric et al. 2011). Because molecular gas and dust are closely connected, we also compare the warm molecular emission properties with PDR models. We use the PDR models of Kaufman et al. (2006), who calculate the [Si II] and H_2 S(0), S(1), S(2), and S(3) pure rotational line emission arising from PDRs in massive star-forming regions.

Kaufman et al. (2006) computed simultaneous solutions for the chemistry, radiative transfer, and thermal balance in PDRs. They assumed that, in the outer layers, the PDR contains singly ionized carbon, silicon, and iron with a temperature greater than 100 K. The observed [Si II] emission at 35 μm is thought to come from this outer layer of PDR. The rotational H_2 transitions (seen in MIR) and the ro-vibrational H_2 lines (seen in NIR) are thought to come from a deeper layer where the H I/H_2 transition is supposed to occur. The resultant emission is a function of the PDR density n and of the incident FUV (6.0 eV $\leqslant h\ \nu \leqslant$ 13.6 eV) flux. The FUV incident radiation is described in terms of G_0: 1.6×10^{-3} erg cm^{-2}, a value comparable to estimates of the local interstellar field in the Milky Way.

Figure 8 shows the combinations of G_0 and density n possible for the observed [Si II] and H_2 flux ratios. We find that our measurements can best be modeled by a PDR/H II model with log (G_0) values between 2.3 and 2.8 and log (n) between 4.1 and 4.6. In Figure 8, we test for systematic differences between: AGN-dominated and non-dominated sources, mergers and isolated galaxies, and targets with resolved H_2 emission versus those without. We find that AGN-dominated sources appear to have a wider range of possible G_0 and density n conditions, similar to the work of Lambrides et al. (2018), who analyze a sample of 2200 active galaxies observed by *Spitzer* IRS and find that AGN-dominated galaxies have a wider range of dust-grain properties.

For two sources, III Zw 35 and NGC 1961, the ratios of S(1) to [Si II] are higher than what can be expected from the PDR models. Those sources are not detected in [O IV], suggesting that if an AGN were present, its MIR emission does not contribute to the overall MIR luminosity of the galaxy because either it is obscured or the AGN is MIR-faint compared to MIR emission from star-forming regions. Carrillo et al. (1999) characterized III Zw 35 as a LINER on the basis of the Veilleux & Osterbrock (1987) classification. Based on its detection in the 2–10 keV X-ray band with Chandra at a level of

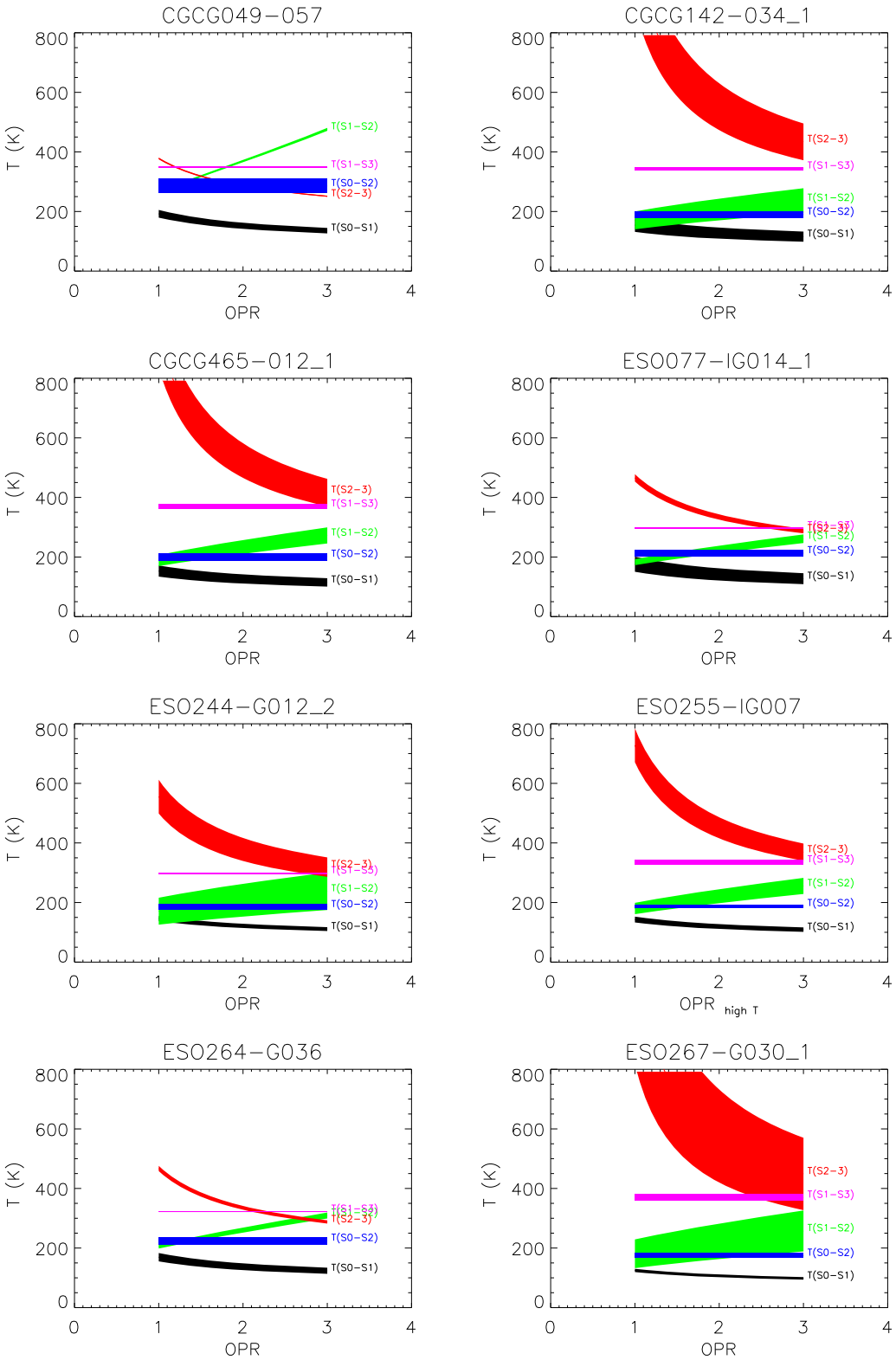

Figure 7. Temperatures as a function of OPR, the thickness of the lines represents the errors associated with the determination of temperature. Here, we provide several examples representative of the observed range of properties.

$(7 \pm 2) \times 10^{-15}$ erg s^{-1} cm^{-2}, as well as on X-ray hardness, it was characterized as a Compton-thick source by González-Martín et al. (2009). Similarly, NGC 1961 is part of the Carrillo et al. (1999) LINER catalog, and was detected with the Einstein X-ray observatory in the 0.2–4.0 keV band at a level of $(7 \pm 3) \times 10^{-13}$ erg s^{-1} cm^{-2} (Fabbiano et al. 1992). The X-ray detections of these LINER galaxies suggest that an XDR model might be more suitable to the data here (Meijerink et al. 2007), and that the sources may be heavily obscured. Both objects are among a small percentage (4%) of LIRGs where we

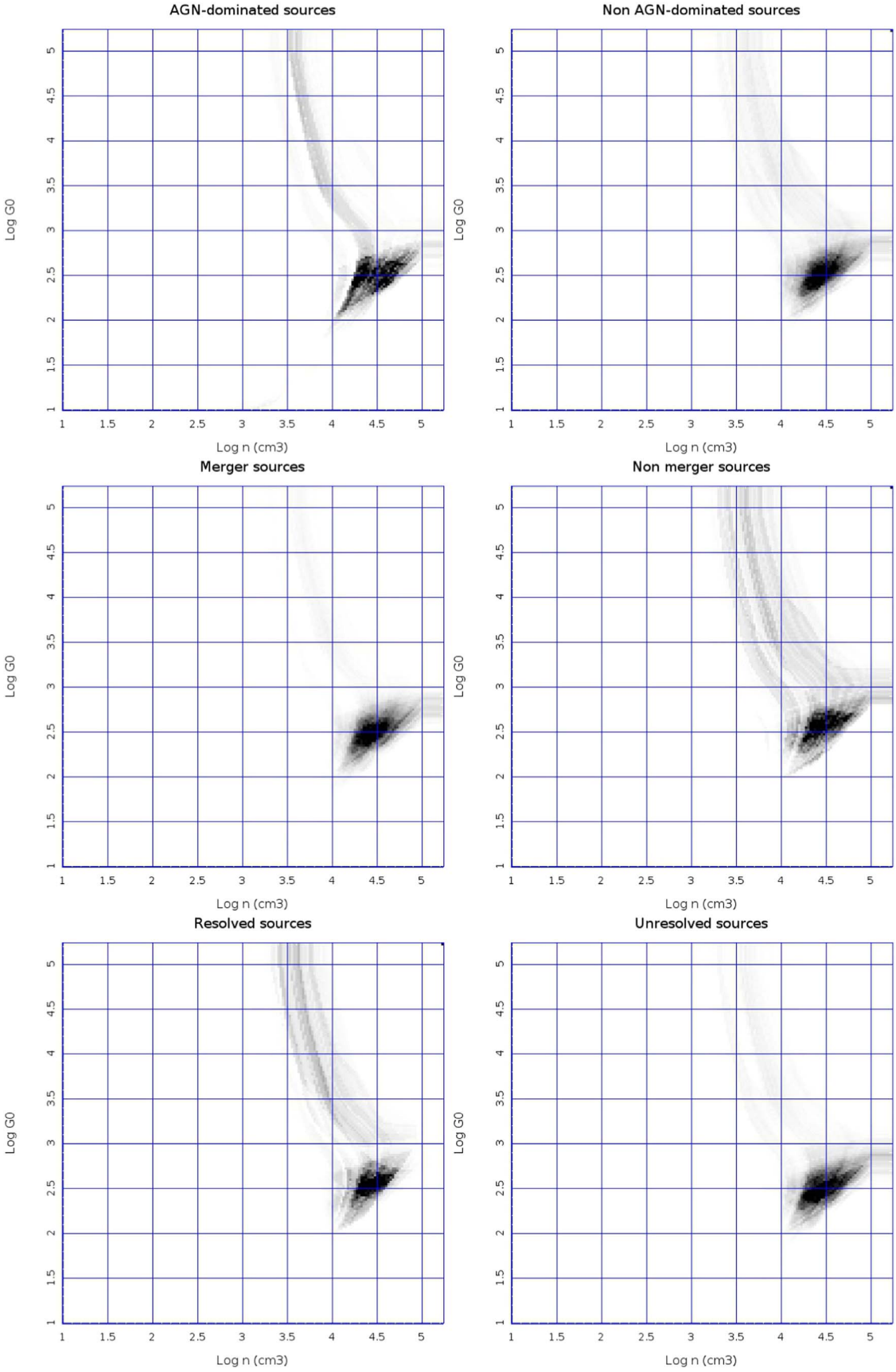

Figure 8. Grayscales showing the most probable region of the (n, G_0) space for: (top) LIRGs with AGNs producing more than 50% of the MIR emission vs. LIRGs in which processes associated with star formation contribute to most of the observed MIR; (middle) LIRGs showing signs of gravitational interactions vs. those without; and (bottom) LIRGs with relatively broad H_2 velocity profiles. These estimates are based on their combined S1/S0, S1/S2, and S1/Si II ratios, as well as on the models of Kaufman et al. (2006) models, and only include detections. See text for details.

detect the H_2 S(5) lines, and their excitation diagrams suggest that the warm molecular gas is not described well by a single temperature.

4. Discussion

Nearby LIRGs appear to have higher H_2/PAH flux ratios than normal star-forming galaxies (Stierwalt et al. 2014). Stierwalt et al. (2014) use simultaneous fits to the dust and gas emission and continuum features in the low-resolution IRS data to determine that around 10% of LIRGs have H_2 emission that is not consistent with PDR models and so could be instead excited by shocks from powerful starbursts or AGN. They also find that L_{H_2}/L_{PAHs} ratios are positively correlated to L_{H_2} and are not correlated with the silicate optical strengths, unlike in ULIRGs (Zakamska 2010). Stierwalt et al. (2014) explain this difference between LIRGs and ULIRGs by suggesting that the excitation mechanisms of warm H_2 outside photodissociation regions, i.e., shocks and AGN, are less common in LIRGs than they are in ULIRGs. Here, we use data at higher spectral resolution to (1) investigate the kinematics of the warm H_2, (2) estimate H_2 masses and temperatures, and (3) use [Si II] and OPR analysis to look at the gas excitation conditions. We discuss theoretical predictions that (1) mergers lead to inflows of gas toward the center and (2) AGN impact the distribution of central molecular gas, through outflows, shocks, and an abundance of cosmic rays.

To compare our measurements of LIRGs to those of normal galaxies and ULIRGs, mergers to non-mergers, and pure starbursts to AGN-dominated sources, we perform statistical tests that rely on both detections and upper limits to determine the probability that two samples are drawn from the same population. The interaction stages we use for this analysis are derived from those used in Petric et al. (2011), and re-analyzed with help from the work of Stierwalt et al. (2013) and Larson et al. (2016) (cf. Haan et al. 2011a; Petty et al. 2014). We use three broad categories: non-mergers, mergers, and early mergers. We call a LIRG AGN-dominated if its 6.2 PAH equivalent width is less than 0.27 and high-ionization [Ne V] is detected or the ratio of [O IV]/[Ne II] is larger than 1.75 (Armus et al. 2007; Veilleux et al. 2009; Petric et al. 2011; Stierwalt et al. 2013).

We used the Astronomy SURVival analysis (ASURV) statistical package (Feigelson & Nelson 1985; Isobe et al. 1986). When we compare flux ratios or fluxes with upper-limits, we present the average probability that the two samples are drawn from the same population using the following five nonparametric tests: (1) the Gehan Generalized Wilcoxon Test using permutation variance, (2) Gehan's Generalized Wilcoxon Test using hypergeometric variance, (3) the Logrank Test, (4) the Peto & Peto Generalized Wilcoxon Test, and (5) the Peto & Prentice Generalized Wilcoxon Test. When we compare kinematics or dust gas masses, we use the Kolmogorov–Smirnov (KS) statistical test. The numbers we provide indicate how different two samples are, based on their cumulative distributions, and the statistical significance of their difference, based on the probability that they are drawn from the same population.

We compare our fluxes and luminosities with those of normal galaxies and ULIRGs. Comparisons using the ratios of S(0) to IR and S(1) to IR are shown in Table 6. We find that the most significant differences are between normal (nearby, non-merging, galaxies discussed in Roussel et al. (2007)) and LIRGs, as well as between LIRGs and ULIRGs (Higdon et al. 2006). The sources investigated by Roussel et al. (2007) are at closer distances and contain fewer sources where the AGN dominates the IR emission than the LIRGs in our sample. Because the normal galaxies presented in Roussel et al. (2007) are closer than the GOALS LIRGs, and because fewer sources in the Roussel et al. (2007) sample are mergers, the IRS spectra probe regions that are of different sizes and may experience different processes.

Table 6
General H_2 Comparisons Using Censored Data Statistical Methods

Samples Compared	$\log (L_{S(0)}/L_{IR})$	$\log (L_{S(1)}/L_{IR})$
ULIRGs versus LIRGs	0%	8%
Normal galaxies versus LIRGs	0%	0%
Merging versus non-merging GOALS galaxies %	90%	68 %
LIRGs with [Ne V] detections versus SB	47%	65%
LIRGs where the AGN dominates the IR versus SB	25%	42%

Note. We give the probability that the two samples are drawn from the same population. This is the average probability we obtain from running each of the following statistical tests, which are especially well-suited for data containing upper limits—also known as censored data: (1) the Gehan Generalized Wilcoxon Test using permutation variance, (2) Gehan's Generalized Wilcoxon Test using hypergeometric variance, (3) the Logrank Test, (4) the Peto & Peto Generalized Wilcoxon Test, and (5) the Peto & Prentice Generalized Wilcoxon Test. Those statistical tests are implemented in the ASURV program by E. Feigelson. Most recently, this program can be also be found at http://www.r-project.org. For the comparisons of mergers versus non-mergers, we also used the 24 μm flux determined by multiplying the LL IRS spectra with the MIPS 24 μm filter as explained in Petric et al. (2011). This was done to test for systematic differences associated with *IRAS* photometry of mergers and non-mergers. Using the 24 micron versus the IR micron luminosity gave us similar results.

4.1. Kinematics as a Function of Interaction Stage, and the AGN Contribution to the L_{IR}

One of the goals of this work is to estimate whether we can identify the kinematic signatures that gravitational interactions and AGN leave on the ISM on kpc scales. To do this, we separated the sources into two groups: 194 LIRGs with unresolved H_2 lines, and 27 sources with resolved and marginally resolved H_2 lines (see Section 3.1.2) to determine whether they are resolved simply because of geometry or they have different H_2 properties. While LIRGs with resolved H_2 lines appear to have more and hotter gas, the results are not highly statistically significant. Table 7 summarizes the statistics presented here.

To test whether the H_2 line broadening may come from rotation of a highly inclined massive galaxy, we visually inspect the 27 sources with resolved and marginally resolved H_2 line profiles in order to see how many appear highly inclined. However, because most sources with broader profiles are mergers and we lack higher-resolution spatial and kinematic information, we cannot properly determine the inclination of the inner few kpc probed by the IRS spectra. ESO 353-G020, UGC 03351, ESO 507-G070, and NGC 7771 could have broader profiles because of rotation: their profile widths are consistent with what we would expect for a spiral of inclination of more than 30° and a mass-to-light ratio on the order of 3.8.

Table 7
General H_2 Comparisons Using the Kolmogorov Smirnov Test

Samples Compared	*DKS* (1)	*PKS* (1)
Sources with resolved H_2 lines versus sources with unresolved H_2 lines		
Masses	0.3	3%
Temperature	0.2	11%
Merger stage	0.2	13%
All mergers versus all non-mergers		
Warm gas masses	0.1	44%
Temperature of warm gas	0.2	7%
Advanced mergers versus all non-mergers		
Warm gas masses	0.3	3%
Temperature of warm gas	0.3	3%
AGN-dominated versus starburst-dominated		
Warm gas masses	0.3	2%
Temperature of warm gas	0.4	0.1%

Note. (1) The Kolmogorov–Smirnov statistic *DKS* gives an estimate of the difference between two distributions of measurements. It does this by comparing the cumulative cumulative distribution functions between the two sets of values being compared. *DKS* = maximum (cumulative distribution of sample 1 − cumulative distribution of sample 2). A cumulative distribution (plotted on the vertical axis) gives the probability that the variable takes a value less than a certain value (shown in the *x*-axis). A small *DKS* (e.g., lower than 0.1) means that the sample properties are similar, while a large *DKS* means that they may be different. To determine whether the *DKS* is statistically significant, we calculate the *PKS,* which gives the probability that the two sets of values compared are drawn from the same population.

Differences between the H_2 S(1) to [Si II] flux ratios of resolved and unresolved sources would indicate differences in excitation conditions because of different radiation fields strengths, spectral shapes, or overall densities. The marginally resolved sources appear to have above-average H_2 luminosities relative to both the 6.2 μm PAH emission and the [Si II] emission. Our small sample of resolved sources makes it difficult to extract statistically significant conclusions. However, we provide this analysis for completeness.

Guillard et al. (2012) find resolved H_2 lines in radio galaxies, Dasyra & Combes (2011) find them in optically selected AGN, and Ogle et al. (2012) find them in $z \sim 2$ radio galaxies. Here, we wish to test whether the AGNs at the cores of LIRGs also impact the surrounding ISM. From our sample of LIRGs with broad H_2 lines, only two sources show detectable [Ne V] at 14.3 μm emission. However, these objects show low [Ne V]/[Ne II] ratios of 0.08 and 0.05, with an average AGN contribution to the total IR luminosity (∼8–1000 μm) of 13%, which is the same as the mean of the entire sample of LIRGs (Petric et al. 2011). The S(1) line widths we measure for LIRGs are lower than those observed in powerful radio galaxies or ULIRGs.

Supermassive black holes at the centers of spheroidal galaxies can supply more energy to the galaxy than the binding energy of the galaxy, even when they grow slowly and have a low feedback efficiency (Hopkins et al. 2006). In simulations, AGNs in gas-rich mergers produce molecular gas outflows; when the outflows have components on the direction of our line of sight, they can be observed as kinematic features such as broad and/or asymmetric emission-line profiles (Narayanan et al. 2006). Assuming that the viewing geometries

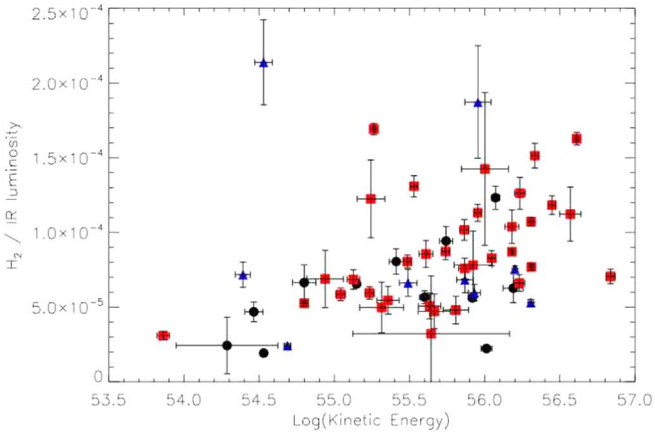

Figure 9. The estimated kinetic energy in the warm H_2 gas correlates well with the ratio of $L_{H_2S(1)}$ to L_{IR} for non-mergers (black circles), early-stage mergers (blue triangles), and advanced mergers (red squares).

of ULIRGs and LIRGs are not statistically different, we would expect that the fraction of ULIRGs with AGN and broad H_2 lines should be similar to that of LIRGs, yet we find relatively fewer LIRGs with broad H_2 profile. Fewer LIRGs than ULIRGs have AGNs that contribute significantly to their host IR, so our observation could indicate low number statistics or suggest that the feedback efficiency is higher in ULIRGs than it is in LIRGs.

Mergers are also known to enhance the H_2 emission (e.g., Guillard et al. 2009, 2012; Peterson et al. 2012), and about 40% of LIRGs are mergers. However, it may be that H_2 emission shocked by the tidal interactions, like that observed in the bridge of the early-stage merger of the Taffy Galaxies (Peterson et al. 2012), was not captured in our nuclear MIR spectroscopic observations, which were focused on the LIRGs nuclei and not the diffuse extended IR emission. The eight galaxies with broad S(0) and S(1) emission profiles appear to be interacting. This may suggest that in LIRGs, shocks associated with tidal interactions are energetically significant and heat the warm molecular gas. For all LIRGs with resolved and marginally resolved H_2 S(1) lines, we approximate the kinetic energy (E_{kin}) of H_2 as $3/2\, M_{H_2}\sigma^2_{H_2}$ where M_{H_2} is the mass of warm H_2 gas (Section 3.2) and σ_{H_2} is the velocity dispersion. We find a statistically significant correlation (i.e., the probability that they are not correlated is 0.04) between the kinetic energy in the H_2 gas and the ratio of $L(H_2S(1))$ to the L_{IR} (Figure 9). While the observed $L(H_2S(1))$ to L_{IR} ratios are compatible with H_2 excitation by UV pumping, we may see evidence for collisional excitation at kinetic energies greater than 10^{55} erg. The sources with the largest warm-gas kinetic energies are mergers.

A possible explanation for our findings is that mergers increase the production of bulk inflows, leading to observable broad H_2 profiles and possibly denser environments and larger masses of warm molecular gas in the central regions of advanced stage mergers than in non-mergers. Outflows associated with the central region can also explain some of the broader profiles. Using the continuum source sizes from Díaz-Santos et al. (2011) and stellar masses of $10^{11}\, M_\odot$, we estimate escape velocities for the gas that range from ∼300 to ∼1000 km s^{-1}. The combination of merger tidal interactions, star formation, and AGN activity in those sources may dramatically affect the overall state of the molecular gas by pushing a fraction of it out of the LIRG. We speculate that,

while outflows may be important, bulk molecular gas inflows may also be present (e.g., Yamashita et al. 2017); those inflows move sufficient gas to the center to fuel star formation and AGN accretion, which lead to turbulence and heating of the molecular gas to 100–1000 K, i.e., the warm gas observed in the MIR. Both inflows and outflows generate turbulence and heat in the molecular gas (Beirão et al. 2015).

One way to contextualize our investigation of H_2 in LIRGs within the study of how AGN and gravitational interactions impact the ISM is to compare it with studies of neutral hydrogen. Gravitational interactions do not appear to significantly affect the ratios of neutral gas to stellar mass in galaxies throughout the merger sequence, and post-mergers may on average be more gas-rich than isolated galaxies (e.g., Ellison et al. 2015). However, interactions may be responsible for the cooling of halo gas and lead to central buildup of molecular gas (e.g., Braine & Combes 1993). Our finding that, in some advanced mergers, the kinetic energy of the warm molecular gas in the central few kpcs is correlated to the ratio of H_2 to IR luminosities is consistent with this scenario. Advanced mergers tend to host more AGN (e.g., Veilleux et al. 2009; Petric et al. 2011) and the ratio of H_2 to PAH luminosity increases with H_2 luminosity in LIRGs (Stierwalt et al. 2014) and in ULIRGs (Hill & Zakamska 2014). Inami et al. (2013) found five nearby LIRGs with asymmetric [Ne III] and [Ne V] emission lines. We do not find any asymmetric H_2 resolved profiles, nor any with significant central velocity shifts, but this may be due to the comparatively lower S/N of the H_2 lines. Spatially resolved NIR spectroscopic studies (e.g., Rupke et al. 2010; Medling et al. 2015) are required to confirm that the the broader MIR profiles are associated with inflow of cooled halo gas.

4.2. Masses and Temperatures as a Function of Interaction Stage, and the AGN Contribution to the L_{IR}

Petric et al. (2011) found there are relatively more AGN-dominated sources among late-stage mergers than there are sources dominated by star formation, compared to non-interacting LIRGs. While we did not find any statistically significant differences between the H_2 masses of mergers and non-mergers, late-stage mergers have the highest warm molecular H_2 masses and temperatures. However, the difference decreases when we normalize the H_2 masses by the IR luminosities, making it difficult to extract strong conclusions from this finding.

When we only use the 128 fits with S(0) detections, we no longer find that late mergers have the highest masses, but we still find that the advanced mergers show higher mass-averaged temperatures. Furthermore, we find that AGN-dominated sources have mass-averaged temperatures about 100 K higher than LIRGs dominated by star formation.

KS tests do not indicate a statistically significant difference between the $L_{\rm IR}/M_{\rm H_2}$ ratios of mergers and those of non-mergers.

The median warm molecular gas mass for sources with an AGN contribution greater than 50% of the total IR luminosity is $2.3 \times 10^7\,M_\odot$; for sources where an AGN contributes less than 10% to the total IR luminosity, it is a few times higher at $1.2 \times 10^8\,M_\odot$. The KS statistical difference between them is 0.3 and the probability that they are drawn from the same population is 2%. The mean and median ratios of $L_{\rm IR}$ to $M_{\rm H_2}$ for AGN-dominated sources are 1.2 and $0.6 \times 10^4\ L_\odot/M_\odot$, and those for starburst-dominated sources are 1.8 and $0.3 \times 10^4\,L_\odot/M_\odot$, with a KS statistic difference between them of 0.17 and a 38% probability that they are the same population. The respective average and median temperatures for AGN-dominated sources are 313 and 296 K, while those of SB-dominated galaxies are 203 and 177 K. The KS statistic differences between the two distributions of temperatures is the largest for any comparison done in the sample, 0.446, with a probability of effectively zero that they are drawn from the same populations.

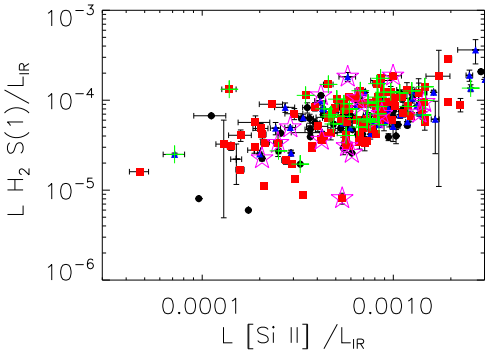

Figure 10. Comparison between the ratios of H_2 S(1) emission to the IR luminosity vs. the ratios of [Si II] to the IR luminosity for non-mergers (black), early-stage mergers (blue), and advanced mergers (red). Sources with resolved and marginally resolved S(1) lines are shown as (green) crosses. Sources with a significant AGN contribution to the total IR luminosity are shown as (magenta) stars.

Statistical differences between the warm gas properties of AGN-dominated LIRGs and those dominated by star formation are more significant than the differences between mergers and non-mergers, and as significant as those between LIRGs and ULIRGs, as well as those between LIRGs and normal-galaxies (Table 7).

4.3. H_2 Excitation Conditions as a Function of Interaction Stage, and the AGN Contribution to the L_{IR}

In Figure 10, we compare the H_2 S(1) emission versus the [Si II] emission, both normalized by the $L_{\rm IR}$ luminosity. This comparison is important because H_2 and [Si II] are both tracers of the warm ISM but their relative intensities vary as a function of the radiation field intensity and the metallicity (Kaufman et al. 2006).

The correlation between the H_2/IR and [Si II]/IR luminosity ratios (Figure 10) suggests that those cooling lines have a common origin for the majority of the sources but that advanced-stage mergers may have more diverse H_2 heating mechanisms. While we do not find statistically significant differences between the [Si II] to H_2 S(1) emission line ratios in mergers from those in non-mergers, mergers have lower median [Si II] to H_2 S(1) emission line ratios (9 versus 12) even though the dispersion is large (five for non-mergers and early-stage mergers and eight for mergers) (Figure 11).

These results confirm those of Peterson et al. (2012), who point out that, while mergers can enhance the total H_2 emission, the observed H_2 properties are highly dependent on the collision geometry and the initial conditions of the mergers. It is thus not surprising that we do not find strong trends with interaction stage or the IR emission.

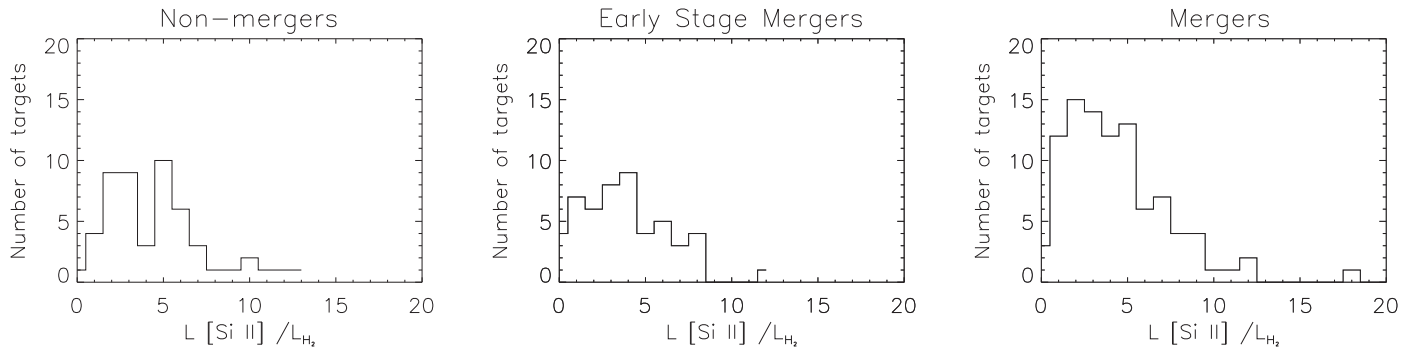

Figure 11. Histograms of [Si II] to H_2 S(1) emission line ratios for: (left) non-mergers, (center) early-stage mergers, and (right) mergers. The standard deviation of the distribution of [Si II] to H_2 S(1) line emission ratios is two times larger for mergers than it is for early-stage mergers and non-mergers. The median [Si II] to H_2 S(1) emission line ratios are ∼12 for non-mergers and ∼9 for mergers.

5. Summary and Conclusions

We present measurements of the rotational transitions of molecular hydrogen observed in a MIR spectroscopic survey of 202 LIRG nuclei with *Spitzer* IRS. We detect H_2 emission in at least one rotational transition in 91% of the sources, S(1) being the most commonly detected transition. The ratio of H_2 S(0) + S(1) + S(2) luminosity to the IR luminosity ranges between 2.3×10^{-6} and 0.014.

We perform a statistical analysis of the S(0) and S(1) lines and their ratios to the IR luminosity, including upper limits, to investigate whether there are systematic differences between the H_2 properties of LIRGs in our sample, normal galaxies as measured by Roussel et al. (2007), and ULIRGs as measured by Higdon et al. (2006). We find that the probability that LIRGs and normal galaxies are drawn from the same population is null, while the probability that LIRGs and ULIRGs are drawn from the same population is 16%. In a similar statistical fashion, we compare the H_2 S(0), S(1), and H_2 [S(1) + S(2)]/L_{IR} for merging versus non-merging LIRGs and for AGN-dominated LIRGs versus those dominated by star formation. We find probabilities of 39% and 30%, respectively, that those samples of galaxies are drawn from the same population.

We compare the ratios of the H_2 lines to the [Si II] line in the context of the theoretical models of PDR/H II regions of Kaufman et al. (2006). Our measurements can be modeled by FUV radiation field values between $10^{2.0}$ and $10^{2.8}$ and hydrogen nucleus densities n between $10^{3.5}$ and $10^{4.5}$ cm^{-3}.

For 78 sources where we detect at least four transitions with high S/N, we investigate whether the temperatures estimated from the S(0), S(1), S(2), and S(3) lines are consistent with an ortho-to-para ratio expected for thermalized gas. For half of the sources, the observed S(0)–S(3) lines suggest that the gas is either non-thermalized or that we are observing emission from regions at different temperatures.

We compute excitation diagrams and use them to estimate the masses and temperatures of warm molecular gas in 214 LIRG nuclei in the GOALS sample. We find that the masses of warm gas in advanced mergers are slightly larger than those of non-interacting systems, and that the statistical differences between the warm gas properties of AGN-dominated sources and non-dominated sources are more significant than the differences between mergers and non-mergers. AGN may power a fraction of the H_2 indirectly through dynamical perturbations that may be responsible for both extensive shocks in the ISM and an increased rate of accretion onto the supermassive black hole. One way to look for the connection between dynamical perturbations and the warm H_2 gas is to look for sign of kinematic peculiarities. In S. Petrus et al. (2018, in preparation), we use data from the Gemini Near Infrared Spectrograph to show that such peculiarities are common among LIRGs with excess H_2 emission.

We find that between 10% and 15% of LIRGs have resolved or marginally resolved S(0) and/or S(1) lines, and that those sources tend to be mergers and have a slightly higher fraction of AGN-dominated sources among them. As was pointed out in Peterson et al. (2012), while mergers can have a significant enhancing effect on the total H_2 luminosity emitted, the observed H_2 properties are highly dependent on the collision geometry and the initial conditions of the mergers. Those sources with resolved lines also tend to have slightly higher H_2/IR luminosity ratios, suggesting either higher G_0 or higher densities. We find a correlation between the kinetic energy in the warm molecular gas and the intrinsic H_2 line widths.

These data, in conjunction with the findings of Ellison et al. (2015) and Yamashita et al. (2017), suggest that the velocity broadening observed in some H_2 profiles may be due to inflow of halo gas that feeds central star formation and the central supermassive black hole, which in turn produce outflows that impart kinetic energy to the central molecular gas. Alternatively, inflows of gas from the galaxies's disk may stimulate star formation and AGN activity, which heat the warm molecular gas to sufficiently high temperatures to be detected via MIR H_2 lines.

Both interpretations are consistent with the narrative of quasar formation that starts with two interacting gas-rich galaxies, passes through an obscured, reddened QSO, and ends with an optically luminous QSO. Those optically luminous QSOs can still have large ISM reservoirs (e.g., Petric et al. 2015) if, as proposed by Braine & Combes (1993), as galaxies merge, hot gas from the halo cools and forms fresh molecular gas on dust grains.

This work is based primarily on observations made with the *Spitzer Space Telescope*, which is operated by the Jet Propulsion Laboratory, California Institute of Technology under NASA contract 1407. We have made use of the NASA/IPAC Extragalactic Database (NED) which is operated by the Jet Propulsion Laboratory, California Institute of Technology, under contract with NASA. Support for this research was provided by NASA through an award issued by JPL/Caltech. V.C. would like to acknowledge partial support from the EU FP7 Grant PIRSES-GA-2012-316788. A.P.

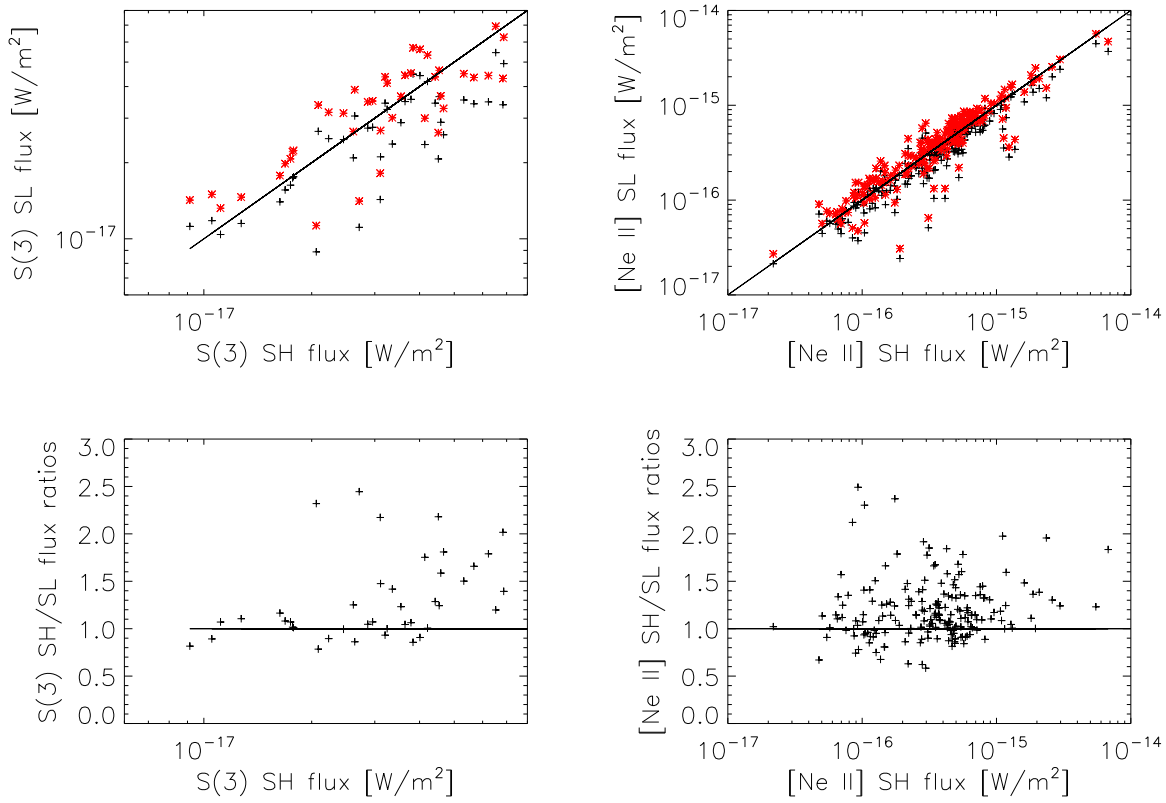

Figure 12. Top left: measured H_2 S(3) line fluxes in SH vs. those measured in SL before scaling. Top right: measured [Ne II] line fluxes in SH vs. those measured in SL before scaling. Red points in both plots show SH measurements vs. the scaled SL fluxes. Black points in both plots show SH measurements vs. measured SL fluxes. Bottom Left: ratio of SH to SL flux estimates of the H_2 S(3) line vs. the flux measured in SH. Bottom Right: ratio of SH to SL flux estimates of the [Ne II] line vs. the flux measured in SH.

thanks T. Geballe for comments that improved the clarity of the paper. N.L. acknowledges support by the NSFC grant #11673028 and National Key R&D Program of China grant #2017YFA0402704.

Appendix A
Matching Apertures

For this investigation of warm molecular H_2 properties, we combined fluxes determined from LH, SH, and SL spectra (Petric et al. 2011; Inami et al. 2013; Stierwalt et al. 2013, 2014). The widths of the SL, SH, and LH slits (3.″7, 4.″7, and 11.″1) correspond to 1.5, 2.0, and 4.6 kpc, respectively, at the median galaxy distance of our sample (88 Mpc).

We scaled each of the LH H_2 S(0) fluxes by comparing the SH and LH spectra. We averaged two scaling factors, called *LH2SHv*1 and *LH2SHv*2 for simplicity. *LH2SHv*1 is the ratio of the median flux in the SH spectra, in the wavelength region overlapping with the LH spectra, to the median flux in the LH spectra, in the wavelength region overlapping with the SH spectra. *LH2SHv*2 is the ratio of the extrapolated flux at 18 μm, from a fit to the continuum of the SH spectra at wavelengths greater than 17.5 μm, to the flux at 18 μm from the LH spectra, derived the same way from data at wavelengths shorter than 20 μm. The linear fit is done by minimizing the absolute differences and not the usual least squares fit; this is important because doing so minimizes the impact of bad pixels that are often found at the edge on the fit. The median value of *LH2SHv*1 is 0.78 and that of *LH2SHv*2 is 0.66; the median of the final scaling factor is 0.72.

For S(3)–S(7) fluxes, we rely on measurements from the lower-resolution SL-spectra. We scale the SL fluxes by the ratio of the spectral extraction widths (4.7/3.7). We compute the error associated with this scaling by looking at the median ratio between the scaled S(3) SL flux and the measured S(3) SH flux. That median relative difference is 25% for S(3). We add this to the error obtained from the Gaussian fits in quadrature. As a test of our method, we apply the same scaling factor to the [Ne II] fluxes derived in SL and compare them with those found in SH. For the [Ne II] lines, we find a scatter associated with these scalings of 20%. Figure 12 shows how the different scaled-up values for SL H_2 S(3) and [Ne II] compared to the values measured in SH, and suggests that our method is reliable at the 20%–25% level. We applied those scaling factors to all SL estimates.

Appendix B
Ortho-to-para Ratios

The OPR value in the high temperature limit (OPR_{highT}), defined as:

$$OPR = OPR_{highT} \frac{\sum_O (2J_O + 1) \exp[-E_O/(kT)]}{\sum_P (2J_P + 1) \exp[-E_P/(kT)]} \quad (6)$$

where o and p refers to ortho (odd) and para (even) states, respectively, I is the spin number, and J is the rotational quantum number, which is equal to 3 in LTE, and allows us to estimate departure from LTE otherwise. If all the observed H_2, is in LTE then T(S0–S1) $\leqslant$ T(S0–S2) $\leqslant$ T(S1–S2) $\leqslant$ T(S1–S3) $\leqslant$ T(S2–S3), as is expected from a Boltzman distribution.

Therefore, the variations of these apparent excitation temperatures as a function of OPR_{highT}, combined with the

condition of monotony, will define a range of OPR_{highT}. If the value of 3 is allowed, then the source is compatible with LTE.

The expression for the excitation temperatures is as follows. T(S0–S2) and T(S1–S3) are independent of OPR_{highT} because they only involve para or ortho levels, and determined directly from the observed fluxes:

$$kT = \frac{E_{u2} - E_{u1}}{\ln(N_{u1}/N_{u2} \times g_{u2}/g_{u1})} \quad (7)$$

However, T(S0–S1), T(S1–S2), and T(S2–S3) depend on OPR_{highT} as follows:

$$k\,T(S_P - S_O) = (E_{u,O} - E_{u,P})/\ln(OPR_{highT}R) \quad (8)$$

with

$$R = F_P/F_O \times A_O/A_P \times \lambda_P/\lambda_O \times (2J_0 + 1)/(2J_P + 1). \quad (9)$$

For each pair $(p, o) = (0, 1)$, $(2, 1)$, and $(2, 3)$, we have computed possible temperatures as a function of OPR_{highT} between 1 and 3. We are able to investigate 78 sources for which the S(0) to S(3) lines were detected and for which the uncertainties of the line flux do not lead to a significantly large uncertainty in the excitation temperature (see Figure 7).

ORCID iDs

Andreea O. Petric https://orcid.org/0000-0003-4030-3455
Nicolas Flagey https://orcid.org/0000-0002-8763-1555
Vassillis Charmandaris https://orcid.org/0000-0002-2688-1956
Sabrina Stierwalt https://orcid.org/0000-0002-2596-8531
Tanio Diaz-Santos https://orcid.org/0000-0003-0699-6083
Nanyao Lu https://orcid.org/0000-0002-8948-1044
Henrik Spoon https://orcid.org/0000-0002-8712-369X
Phil Appleton https://orcid.org/0000-0002-7607-8766
Jason Chu https://orcid.org/0000-0003-3955-2470
George Privon https://orcid.org/0000-0003-3474-1125
David Sanders https://orcid.org/0000-0002-1233-9998
Jason Surace https://orcid.org/0000-0001-7291-0087
Yinghe Zhao https://orcid.org/0000-0002-9128-818X

References

Armus, L., Charmandaris, V., Bernard-Salas, J., et al. 2007, ApJ, 656, 148
Armus, L., Mazzarella, J. M., Evans, A. S., et al. 2009, PASP, 121, 559
Beirão, P., Armus, L., Lehnert, M. D., et al. 2015, MNRAS, 451, 2640
Black, J. H., & Dalgarno, A. 1976, ApJ, 203, 132
Braine, J., & Combes, F. 1993, A&A, 269, 7
Carrillo, R., Masegosa, J., Dultzin-Hacyan, D., & Ordoñez, R. 1999, RMxAA, 35, 187
Cluver, M. E., Appleton, P. N., Boulanger, F., et al. 2010, ApJ, 710, 248
Dasyra, K. M., & Combes, F. 2011, A&A, 533, L10
Dasyra, K. M., Ho, L. C., Armus, L., et al. 2008, ApJL, 674, L9
Díaz-Santos, T., Armus, L., Charmandaris, V., et al. 2014, ApJL, 788, L17
Díaz-Santos, T., Charmandaris, V., Armus, L., et al. 2010, ApJ, 723, 993
Díaz-Santos, T., Charmandaris, V., Armus, L., et al. 2011, ApJ, 741, 32
Ellison, S. L., Fertig, D., Rosenberg, J. L., et al. 2015, MNRAS, 448, 221
Evans, A. S., Vavilkin, T., Pizagno, J., et al. 2008, ApJL, 675, L69
Fabbiano, G., Kim, D.-W., & Trinchieri, G. 1992, ApJS, 80, 531
Feigelson, E. D., & Nelson, P. I. 1985, ApJ, 293, 192
Fernández, X., Petric, A. O., Schweizer, F., & van Gorkom, J. H. 2014, AJ, 147, 74
Flagey, N., Goldsmith, P. F., Lis, D. C., et al. 2013, ApJ, 762, 11
González-Martín, O., Masegosa, J., Márquez, I., Guainazzi, M., & Jiménez-Bailón, E. 2009, A&A, 506, 1107
Guillard, P., Boulanger, F., Pineau des Forêts, G., et al. 2012, ApJ, 749, 158
Guillard, P., Boulanger, F., Pineau Des Forêts, G., & Appleton, P. N. 2009, A&A, 502, 515
Haan, S., Armus, L., Laine, S., et al. 2011a, ApJS, 197, 27
Haan, S., Surace, J. A., Armus, L., et al. 2011b, AJ, 141, 100
Hayward, C. C., Kereš, D., Jonsson, P., et al. 2011, ApJ, 743, 159
Higdon, S. J. U., Armus, L., Higdon, J. L., Soifer, B. T., & Spoon, H. W. W. 2006, ApJ, 648, 323
Hill, M. J., & Zakamska, N. L. 2014, MNRAS, 439, 2701
Hopkins, P. F., Hernquist, L., Cox, T. J., et al. 2006, ApJS, 163, 1
Huber, K. P., & Hertzberg, G. 1979, Constants of Diatomic Molecules (New York: Van Nostrand)
Inami, H., Armus, L., Charmandaris, V., et al. 2013, ApJ, 777, 156
Inami, H., Armus, L., Surace, J. A., et al. 2010, AJ, 140, 63
Isobe, T., Feigelson, E. D., & Nelson, P. I. 1986, ApJ, 306, 490
Kaufman, M. J., Wolfire, M. G., & Hollenbach, D. J. 2006, ApJ, 644, 283
Kewley, L. J., Rupke, D., Zahid, H. J., Geller, M. J., & Barton, E. J. 2010, ApJL, 721, L48
Lambrides, E. L., Petric, A. O., Tchernyshyov, K., Zakamska, N. L., & Watts, D. J. 2018, MNRAS, submitted, arXiv:1808.02035
Larson, K. L., Sanders, D. B., Barnes, J. E., et al. 2016, ApJ, 825, 128
Mazzarella, J. M., Iwasawa, K., Vavilkin, T., et al. 2012, AJ, 144, 125
Medling, A. M., U, V., Rich, J. A., et al. 2015, MNRAS, 448, 2301
Meijerink, R., Spaans, M., & Israel, F. P. 2007, A&A, 461, 793
Mihos, J. C., & Hernquist, L. 1996, ApJ, 464, 641
Modica, F., Vavilkin, T., Evans, A. S., et al. 2012, AJ, 143, 16
Narayanan, D., Cox, T. J., Robertson, B., et al. 2006, ApJL, 642, L107
Ogle, P., Boulanger, F., Guillard, P., et al. 2010, ApJ, 724, 1193
Ogle, P., Davies, J. E., Appleton, P. N., et al. 2012, ApJ, 751, 13
Patton, D. R., Torrey, P., Ellison, S. L., Mendel, J. T., & Scudder, J. M. 2013, MNRAS, 433, L59
Peterson, B. W., Appleton, P. N., Helou, G., et al. 2012, ApJ, 751, 11
Petric, A. O., Armus, L., Howell, J., et al. 2011, ApJ, 730, 28
Petric, A. O., Ho, L. C., Flagey, N. J. M., & Scoville, N. Z. 2015, ApJS, 219, 22
Petty, S. M., Armus, L., Charmandaris, V., et al. 2014, AJ, 148, 111
Privon, G. C., Barnes, J. E., Evans, A. S., et al. 2013, ApJ, 771, 120
Privon, G. C., Herrero-Illana, R., Evans, A. S., et al. 2015, ApJ, 814, 39
Psychogyios, A., Charmandaris, V., Diaz-Santos, T., et al. 2016, A&A, 591, A1
Roussel, H., Helou, G., Hollenbach, D. J., et al. 2007, ApJ, 669, 959
Rupke, D. S. N., Kewley, L. J., & Barnes, J. E. 2010, ApJL, 710, L156
Sanders, D. B., Mazzarella, J. M., Kim, D.-C., Surace, J. A., & Soifer, B. T. 2003, AJ, 126, 1607
Sanders, D. B., & Mirabel, I. F. 1996, ARA&A, 34, 749
Smith, J. D. T., Armus, L., Dale, D. A., et al. 2007a, PASP, 119, 1133
Smith, J. D. T., Draine, B. T., Dale, D. A., et al. 2007b, ApJ, 656, 770
Spoon, H. W. W., Marshall, J. A., Houck, J. R., et al. 2007, ApJL, 654, L49
Springel, V. 2000, MNRAS, 312, 859
Stierwalt, S., Armus, L., Charmandaris, V., et al. 2014, ApJ, 790, 124
Stierwalt, S., Armus, L., Surace, J. A., et al. 2013, ApJS, 206, 1
Veilleux, S., & Osterbrock, D. E. 1987, ApJS, 63, 295
Veilleux, S., Rupke, D. S. N., Kim, D.-C., et al. 2009, ApJS, 182, 628
Yamashita, T., Komugi, S., Matsuhara, H., et al. 2017, ApJ, 844, 96
Zakamska, N. L. 2010, Natur, 465, 60